HHS Public Access

Author manuscript

J Neural Eng. Author manuscript; available in PMC 2019 April 01.

Published in final edited form as:

J Neural Eng. 2018 April 01; 15(2): 026003–. doi:10.1088/1741-2552/aa8b7c.

Modified cable equation incorporating transverse polarization of neuronal membranes for accurate coupling of electric fields

Boshuo Wang[1], **Aman S. Aberra**[2], **Warren M. Grill**[2,3,4,5], and **Angel V. Peterchev**[1,2,3,5,*]

[1]Department of Psychiatry and Behavioral Science, School of Medicine, Duke University, Durham, NC 27710, USA

[2]Department of Biomedical Engineering, Pratt School of Engineering, Duke University, Durham, NC 27708, USA

[3]Department of Electrical and Computer Engineering, Pratt School of Engineering, Duke University, Durham, NC 27708, USA

[4]Department of Neurobiology, School of Medicine, Duke University, Durham, NC 27710, USA

[5]Department of Neurosurgery, School of Medicine, Duke University, Durham, NC 27710, USA

Abstract

Objective—We present a theory and computational methods to incorporate transverse polarization of neuronal membranes into the cable equation to account for the secondary electric field generated by the membrane in response to transverse electric fields. The effect of transverse polarization on nonlinear neuronal activation thresholds is quantified and discussed in the context of previous studies using linear membrane models.

Approach—The response of neuronal membranes to applied electric fields is derived under two time scales and a unified solution of transverse polarization is given for spherical and cylindrical cell geometries. The solution is incorporated into the cable equation re-derived using an asymptotic model that separates the longitudinal and transverse dimensions. Two numerical methods are proposed to implement the modified cable equation. Several common neural stimulation scenarios are tested using two nonlinear membrane models to compare thresholds of the conventional and modified cable equations.

Main results—The implementations of the modified cable equation incorporating transverse polarization are validated against previous results in the literature. The test cases show that transverse polarization has limited effect on activation thresholds. The transverse field only affects thresholds of unmyelinated axons for short pulses and in low-gradient field distributions, whereas myelinated axons are mostly unaffected.

Significance—The modified cable equation captures the membrane's behavior on different time scales and models more accurately the coupling between electric fields and neurons. It addresses the limitations of the conventional cable equation and allows sound theoretical interpretations. The implementation provides simple methods that are compatible with current simulation approaches

*Corresponding authors: angel.peterchev@duke.edu.

to study the effect of transverse polarization on nonlinear membranes. The minimal influence by transverse polarization on axonal activation thresholds for the nonlinear membrane models indicates that predictions of stronger effects in linear membrane models with a fixed activation threshold are inaccurate. Thus, the conventional cable equation works well for most neuroengineering applications, and the presented modeling approach is well suited to address the exceptions.

Keywords

electromagnetic–neuronal coupling; cable equation; transverse electric field; transverse polarization; activation threshold

1. Introduction

Accurate modeling of neuronal activation by an exogenous electric field (E-field) enables understanding of neural stimulation mechanisms as well as optimization of stimulus parameters. The cable equation (CE) is commonly used to couple extracellular fields to neuronal models [1–7], and has been explored for many conditions, including unmyelinated versus myelinated axons [2,8], unlimited versus limited extracellular space [4], frequency dependence [9], and inductive magnetic stimulation [6]. Three major mechanisms of membrane polarization can be derived from the CE: the activating function, i.e., the spatial gradient of the applied E-field in the axial direction, polarization at axonal and dendritic terminals proportional to the axial E-field [10], and polarization at discontinuities of tissue electrical properties [11]. To represent extracellular stimulation, the CE is coupled with the extracellular E-field, which is typically calculated from simple analytical expressions or complex macroscopic finite element models (FEM). This two-stage approach [12] has been used in a wide range of applications, e.g., epidural cortical stimulation [13], spinal cord stimulation [14], retinal prosthesis [15], cochlear implants [16], and magnetic stimulation [17,18].

The conventional CE, however, is an approximation used to describe the changes in transmembrane potential generated by exogenous E-fields. The axon is represented as a one-dimensional (1-D) line, and the applied E-field is coupled unidirectionally to the axon. This simplifies the model and allows easy computational implementation. However, the mutual interactions between the applied field and neural membrane are absent and some aspects of membrane polarization are not captured. Krassowska and Neu [19] provided a theoretical foundation to include the interaction of the neuronal membrane with the applied field and showed that the cell membrane responds to an imposed extracellular E-field over two distinct time scales. The fast response is transverse polarization (TP) that rapidly and differentially polarizes the membrane from its mean potential. TP is also termed initial polarization [19] when the whole neuron is considered as a single compartment with simple compact morphology. In neuronal cables or morphologically realistic neurons, TP is only present locally across the cable due to the small size and low intracellular impedance in the transverse dimension. The slower response is the change in the mean membrane potential, which reflects the state of the neuron via subthreshold behaviors and suprathreshold action potentials [19], and can be modeled by the CE [20].

Since TP could potentially affect the threshold for neural activation, many modeling studies argued for the necessity to include TP for accurate simulations and developed sophisticated mathematical and computational tools toward this goal [4,12,19–40]. These approaches can be generally divided into two categories, each having certain limitations. The first method solves analytically for membrane behavior in simple geometries. Explicit solutions of TP in uniform E-fields are available for cylindrical cells (in 2-D cross section) [19,21,22] and spherical cells (3-D) [4,22]. For more complex situations, the numerical approximation of the analytical solutions can be calculated, e.g., for spheroidal cells in uniform field [23,24], spherical cells in non-uniform fields [25], infinite axon with point source [26–29] or arbitrary field distribution [30,31], spherical and cylindrical cells in an E-field induced by off-axis harmonic magnetic field [32,33], and clustering of cell bodies and axons [34–36]. One limitation of this approach is the restriction to only single compartments or to axons under subthreshold conditions. For the former, both linear and nonlinear behaviors were included; however, single compartments cannot represent activation of complex neuronal structures by transverse fields. On the other hand, the distributed models used changes in linear membrane polarization to predict the effect of TP on suprathreshold behavior assuming a fixed activation threshold (see sections 3.2 and 4.3). As we will demonstrate herein, such predictions showing a strong influence of TP appear to be inaccurate. Another limitation of this approach is that an unmyelinated axon is necessary to derive differential equations and continuous analytical solutions, whereas many applications involve myelinated axons. The second approach employs FEM of neuronal structures and can include nonlinear membranes and complex geometries [12,21,37–39]. These simulations confirmed the TP theory and enabled modeling of complex behaviors, including ephaptic coupling [38,39]. However, the complex geometries require large and dense meshes, which are further complicated by the broad range of spatial scales, resulting in high computational costs. Additionally, to resolve the large capacitive membrane current during TP, very short time steps (10–50 ns) are required. By contrast, the typical time step for CE solvers like NEURON [41] is typically on the order of tens of microseconds [42]. Therefore, this method only explored simple geometries (often with a linear membrane) and did not systematically study the effect of TP on activation thresholds.

To address the limitations of prior models, we propose a modified CE that includes the effects of TP based on an asymptotic model [20] that decomposes the 3-D geometry of a nerve fiber into a 1-D longitudinal equation and a 2-D transverse equation. The longitudinal problem is the conventional CE and the transverse problem includes TP. The asymptotic model avoids some of the limitations of the aforementioned analytical approach. However, the 2-D transverse problem is a set of partial differential equations that is dependent on the longitudinal CE and still requires sub-microsecond time steps for solution. Adopting dimensional decomposition and assuming a uniform field for the transverse problem, the proposed modified CE directly incorporates the transverse solution into the longitudinal CE, thus overcoming the limitations of the 1-D CE while preserving compatibility with current CE solvers. There are no additional computational costs in the time domain and the increase in the spatial domain is negligible compared to complex FEM simulations.

We first summarize the analytical results of TP from the literature and then re-derive the CE to include TP. We describe two numerical techniques for practical implementation of the

modified CE with nonlinear membrane properties. The linearized version is validated against analytical results and demonstrates that the assumption of uniform transverse field is valid for a wide range of applications. To determine whether TP affects neuronal activation as predicted by previous linear solutions, nonlinear models are included in several test cases, including axon terminals and bends as well as several electrical stimulation configurations. The Hodgkin-Huxley (HH) model [43] and the Richardson-McIntyre-Grill (RMG) model [44] are used to represent unmyelinated and myelinated axons, respectively. The results reveal that TP is relevant for stimulation paradigms that have short pulse durations and/or low spatial gradients of the applied E-field. TP can be neglected for most applications of electrical stimulation, especially when activating myelinated axons. The modified CE provides a simple solution to study the effect of TP on nonlinear membranes, whereas linear models appear insufficient to determine neuronal activation thresholds.

2. Theoretical framework

2.1. Transverse polarization of cylindrical and spherical cell elements

In response to an applied E-field, neurons first undergo transverse polarization (TP), during which the membrane rapidly redistributes charge within the intra- and extra-cellular spaces to establish a secondary field without changing its mean membrane potential. The mathematical analysis and interpretation of TP was thoroughly described by Krassowska and Neu [19] for arbitrarily shaped cells and explicit solutions were given for some regular cell shapes [4,19,21]. Because TP is fundamental for modifying the CE to include this rapid response of neural membranes, this section first presents a unified analysis and relevant results for cylindrical (2-D) and spherical (3-D) cells based on the literature. For simplicity, but without loss of generality, in the following text these two geometries are sometimes referred to as axon or axonal segments and cell body or soma, respectively.

2.1.1. Cellular parameters and coordinate system—The radius of an axon or soma is defined as R. The membrane has specific capacitance c_{m} and specific resistance r_{m} and its thickness is neglected. Homogeneous and isotropic conductivities $\sigma_{\mathrm{i,e}}$ are assumed in the intra- and extra-cellular space, corresponding to subscripts i and e, respectively. The coordinate system is shown in Figure 1. For axons, a cylindrical coordinate system is used with the z-axis along the center of the axon and the reference direction (x-axis) defined by the transverse projection of the E-field. The radial coordinate is ρ and the azimuthal angle is θ, in accordance with 2-D polar coordinates. For somas, a spherical coordinate system is used with the polar axis aligned in the direction of the E-field and set as the x-axis for consistency with axons. The radial coordinate is also ρ and the polar angle is θ. Due to the rotational symmetry of the soma with respect to the field orientation, the y and z-axes and azimuth ϕ do not appear in the analysis.

2.1.2. System of equations for electric field and potentials—An E-field of strength $E_{\mathrm{x}}^{'}$ is applied at $t = 0^{+}$

$$\overrightarrow{E^{'}} = E_{\mathrm{x}}^{'} \cdot \hat{x} \cdot u(t), \quad (1)$$

with $\hat{x}$ being the unit vector in the x-direction, $u(t)$ being the unit step function, and the prime indicating primary field (the terms *primary*, *exogenous*, and *applied* are used interchangeably). Here, the E-field is assumed to be spatially uniform, as non-uniformities appear on spatial scales larger than the local cellular structure in the transverse dimensions (further discussed in section 2.1.4). The intra- and extra-cellular potentials are defined as $\varphi_{\mathrm{i,e}}$, and include the contributions of the source (primary) and the response from the membrane (secondary), i.e., $\varphi_{\mathrm{i,e}}=\varphi'_{\mathrm{i,e}}+\varphi''_{\mathrm{i,e}}$. Laplace's equation applies as there are no free-charge sources

$$\nabla \cdot \sigma_{\mathrm{i,e}} \nabla \varphi_{\mathrm{i,e}}=0. \quad (2)$$

The transmembrane potential φ_{m} is given as

$$\varphi_{\mathrm{m}}=\varphi_{\mathrm{i}}\big|_{\rho=R^-}-\varphi_{\mathrm{e}}\big|_{\rho=R^+}=\varphi''_{\mathrm{i}}\big|_{\rho=R^-}-\varphi''_{\mathrm{e}}\big|_{\rho=R^+}; \quad (3)$$

because the primary potential field is continuous on the boundary and yields no membrane polarization. On the time scale of interest, the intra- and extra-cellular current densities are continuous at the membrane and equal to the membrane current density i_{m}

$$-\sigma_{\mathrm{i}} \nabla \varphi_{\mathrm{i}} \cdot \hat{\rho}=-\sigma_{\mathrm{e}} \nabla \varphi_{\mathrm{e}} \cdot \hat{\rho}=i_{\mathrm{m}}, \quad (4)$$

with $\hat{\rho}$ being the unit vector in the radial direction. The membrane current includes capacitive and ionic components

$$i_{\mathrm{m}}=c_{\mathrm{m}} \frac{\partial \varphi_{\mathrm{m}}}{\partial t}+\sum_j g_{\mathrm{m}}^{(j)}(\varphi_{\mathrm{m}}) \cdot \left(\varphi_{\mathrm{m}}-\mathscr{E}^{(j)}\right), \quad (5)$$

where the summation is over all ion channels, each having reversal potential $\mathscr{E}^{(j)}$ and transmembrane-potential-dependent conductance $g_{\mathrm{m}}^{(j)}(\varphi_{\mathrm{m}})$, respectively, with j indexing different types of channels. For the rest of section 2.1, φ_{i} and φ_{m} are taken as reduced potentials, i.e., small-signal perturbations from the resting potential V_{r}, and only subthreshold behaviors with linear leakage (L) channels are considered, i.e., $\mathscr{E}^{\mathrm{L}}=V_{\mathrm{r}}$ and $g_{\mathrm{m}}^{\mathrm{L}}=r_{\mathrm{m}}^{-1}$. Hence

$$i_{\mathrm{m}}=c_{\mathrm{m}} \frac{\partial \varphi_{\mathrm{m}}}{\partial t}+\frac{\varphi_{\mathrm{m}}}{r_{\mathrm{m}}}. \quad (6)$$

2.1.3. Unified solution for axon and soma—To arrive at a unique solution, the potentials must be referenced to an arbitrary value. This process, also termed normalization [19], can be conveniently accomplished by specifying the mean extracellular potential

$$\overline{\varphi}_{\mathrm{e}} \triangleq \frac{1}{S}\oiint_{r=R^{+}} \varphi_{\mathrm{e}}\mathrm{d}S=\frac{1}{S}\oiint_{r=R^{+}} \varphi_{\mathrm{e}}^{'}\mathrm{d}S=\overline{\varphi}_{\mathrm{e}}^{'}, \tag{7}$$

where dS and S are the surface unit for integration and the total surface area of the membrane, respectively. As there are no sources of charge, the cell behaves as a dipole (multipole for irregular shapes) during TP, and the integration is the same if calculated only for the primary source field without accounting for the presence of the cell. The normalization is set to zero for simplicity in the initial analysis, i.e., $\overline{\varphi}_{\mathrm{e}}=\overline{\varphi}_{\mathrm{e}}^{'}=0$.

The TP problem was described several times in the literature and a derivation is given in Appendix I. The potentials and current density in the system follow a first-order solution with a time constant τ_{TP} (defined by (27) and (28)), and the steady state solution is approximately

$$\begin{cases} \varphi_{\mathrm{i}} \approx 0=\overline{\varphi}_{\mathrm{e}}^{'} \\ \varphi_{\mathrm{e}} \approx -E_{\mathrm{x}}^{'}\cos\theta\left(\rho+\frac{R^{n_{\mathrm{D}}+1}}{n_{\mathrm{D}}\rho^{n_{\mathrm{D}}}}\right), \quad t \gg \tau_{\mathrm{TP}} \\ \varphi_{\mathrm{m}} \approx E_{\mathrm{x}}^{'}R\cos\theta\left(1+\frac{1}{n_{\mathrm{D}}}\right) \end{cases}. \tag{8}$$

Here, the parameter n_{D} is related to the dimension of the neuronal structure and is 1 for cylindrical cells and 2 for spherical cells. The steady state is reached in approximately 5 to 6 time constants, which is less than 1 μs for typical cellular parameters yielding $\tau_{\mathrm{TP}} \approx$ 10–100 ns. The dynamics of TP are much shorter than the resting membrane time constant (1 ms) and the typical time step (10 μs) used in CE solvers. It is also shorter than the time scale on which the E-field changes in typical neurostimulation applications, and the discontinuities at pulse onset and offset are already accounted for by the step function in (1).

Two important conclusions follow from the steady state solution of TP. First, although φ_{i} is spatially uniform and equal to the mean extracellular potential outside the compartment, (8) shows that φ_{m} is amplified compared to the value calculated by considering only the extracellular potential from the applied E-field, i.e., $E_{\mathrm{x}}^{'}R\cos\theta$. This increase, by a factor of $1/n_{\mathrm{D}}$, is due to the secondary field $\varphi_{\mathrm{e}}^{''}$ of the cell membrane. Accordingly, the cylindrical and spherical geometries increase φ_{m} by 100% and 50%, respectively (effect of cell clustering is discussed in section 5.2). Second, on time scales longer than TP but shorter than physiological activity, the membrane insulates the intracellular space from the exogenous field, and current flow generated by external stimuli is confined to the extracellular space. The membrane charge redistribution by TP does not affect the neutrality of the neuronal compartment (see Appendix I), and the dipole-like influence of its secondary field in the extracellular space is insignificant beyond a few radii. The compartments contribute no net current to the extracellular space during TP and become sources or sinks only on physiological time scales due to axial current between adjacent compartments and activation of nonlinear ion channels.

2.1.4. Generalization of transverse polarization solution for axons—The solution and implications of TP are now generalized beyond some of the assumptions used during the derivation for single compartments. First, the uniformity of the exogenous field is relaxed using the asymptotic model [20] to decouple the 3-D system of equations into a 1-D longitudinal equation and a 2-D transverse equation. As exogenous fields have negligible spatial variations on microscopic scales, the transverse problem can be approximated by the cosine-dependent TP solution for uniform fields [20,25,26,29]. A more rigorous analysis is given in Appendix I, and numerical validation is shown in section 3.2. Axons can extend over long distances and the spatial variation of the exogenous field in the longitudinal direction affects the local transverse solution, which is taken into consideration by setting the normalization for each axonal segment as

$$\overline{\varphi}_{\mathrm{e}}^{'}(z)=-\int \overline{E}_{\mathrm{z,e}}^{'}\mathrm{d}z, \quad (9)$$

in which the z-direction is the local axial direction and $\overline{E}_{\mathrm{z,e}}^{'}$ is the axial component of the extracellular E-field averaged around the membrane circumference at a given axial location (calculated similarly to (7)).

Second, for time variation of the applied E-field on scales larger than τ_{TP}, the normalization condition (9) contains a time dependence and therefore the extracellular potential for axons is given as

$$\varphi_{\mathrm{e}}(z,R,\theta,t)=\overline{\varphi}_{\mathrm{e}}^{'}(z,t)-2E_{\mathrm{x}}^{'}(z,t)R\cos\theta. \quad (10)$$

The intracellular potential is spatially uniform after the brief TP and evolves on slower temporal scales with electrophysiological activity [19]. Although the local membrane time constant may decrease into the range of 10 μs during action potentials, TP is still two orders of magnitude faster. Therefore, the spatial uniformity of φ_{i} is valid when a nonlinear membrane is considered and the intra- and extracellular potentials are uncoupled, i.e., $\varphi_{\mathrm{i}}(z,t)\neq\overline{\varphi}_{\mathrm{e}}^{'}(z,t)$. The transmembrane potential is given as

$$\varphi_{\mathrm{m}}(z,\theta,t)=\overline{\varphi}_{\mathrm{m}}(z,t)+2E_{\mathrm{x}}^{'}(z,t)R\cos\theta. \quad (11)$$

in which $\overline{\varphi}_{\mathrm{m}}=\varphi_{\mathrm{i}}-\overline{\varphi}_{\mathrm{e}}^{'}$ is the average membrane potential for a given axial location.

2.2. Modified cable equation with transverse polarization

In this section, the time scale is longer than τ_{TP}, which is true for typical applications of neural stimulation. In the following derivation, φ_{i} and φ_{m} are absolute, not reduced, potentials, so that $\varphi_{\mathrm{m}}=\varphi_{\mathrm{i}}-\varphi_{\mathrm{e}}$ can be used directly to calculate channel conductance as in (5). All considerations in section 2.1.4 are applicable, so that the spatial and temporal variation of the applied field and the change in the physiological state are included.

The first step in deriving the CE is to consider the axial current driven by the intracellular field

$$I_{\mathrm{i}}=\sigma_{\mathrm{i}}\int_0^{2\pi}\int_0^{R^-}E_{z,\mathrm{i}}\rho\mathrm{d}\rho\mathrm{d}\theta. \quad (12)$$

The axial field strength is spatially uniform, given uniform φ_{i} at any transverse plane after TP. Hence

$$R_{\mathrm{i}}I_{\mathrm{i}}=-\frac{\partial\varphi_{\mathrm{i}}}{\partial z}, \quad (13)$$

where $R_{\mathrm{i}}=(\sigma_{\mathrm{i}}\pi R^2)^{-1}$ is the axial resistance per unit length.

The spatial derivative of I_{i} in the axial direction under zero source (2) and current continuity (4) conditions yields

$$\frac{\partial I_{\mathrm{i}}}{\partial z}=-\sigma_{\mathrm{i}}\int_0^{2\pi}\int_0^{R^-}\left(\frac{\partial(\rho E_{\rho,\mathrm{i}})}{\partial\rho}+\frac{\partial E_{\theta,\mathrm{i}}}{\partial\theta}\right)\mathrm{d}\rho\mathrm{d}\theta=-\int_0^{2\pi}\sigma_{\mathrm{i}}(\rho E_{\rho,\mathrm{i}})\big|_{\rho=R^-}\mathrm{d}\theta=-R\int_0^{2\pi}i_{\mathrm{m}}(\theta)\mathrm{d}\theta. \quad (14)$$

In this derivation, the radial and azimuthal components of the intracellular E-field are involved and are non-zero, especially for $E_{\rho,\mathrm{i}}$ to yield a non-zero membrane current density. Although appearing contradictory to the condition of zero intracellular transverse field at steady state of TP, the strength of this field is negligible as the primary field is *almost* cancelled out by the membrane's secondary field (see (29) and Figure 10 in Appendix I). Compared to the primary and secondary fields, the total field in (14) is a small residual that is sufficient to drive the current densities involved in neural activity. This has been demonstrated by FEM [38] in which the simulated membrane current density declined by at least two orders of magnitude throughout the TP process.

Unlike the conventional CE, the membrane current varies around the circumference of the axon segment. Due to the cosine dependence of φ_{m} on θ as given in (11), the ionic current is symmetric for the $[0, \pi]$ and $[\pi, 2\pi]$ intervals of θ and the capacitive current can be simplified with $\int_0^{2\pi}\varphi_{\mathrm{m}}(\theta)\mathrm{d}\theta=2\pi\overline{\varphi}_{\mathrm{m}}$. Therefore, (14) becomes

$$-\frac{\partial I_{\mathrm{i}}}{\partial z}=2\pi Rc_{\mathrm{m}}\frac{\partial\overline{\varphi}_{\mathrm{m}}}{\partial t}+2R\sum_j\int_0^{\pi}g_{\mathrm{m}}^{(j)}\left(\overline{\varphi}_{\mathrm{m}}+2E_{\mathrm{x}}^{'}R\cos\theta\right)\cdot\left(\overline{\varphi}_{\mathrm{m}}+2E_{\mathrm{x}}^{'}R\cos\theta-\mathscr{E}^{(j)}\right)\cdot\mathrm{d}\theta. \quad (15)$$

Substituting the axial current with (13) and $\varphi_{\mathrm{i}}=\overline{\varphi}_{\mathrm{m}}+\overline{\varphi}_{\mathrm{e}}^{'}$, the modified CE is obtained

$$c_{\mathrm{m}}\frac{\partial\overline{\varphi}_{\mathrm{m}}}{\partial t}+\frac{1}{\pi}\sum_{j}\int_{0}^{\pi}g_{\mathrm{m}}^{(j)}\left(\overline{\varphi}_{\mathrm{m}}+2E_{\mathrm{x}}^{'}R\cos\theta\right)\cdot\left(\overline{\varphi}_{\mathrm{m}}+2E_{\mathrm{x}}^{'}R\cos\theta-\mathscr{E}^{(j)}\right)\cdot\mathrm{d}\theta=\frac{1}{2\pi R\cdot R_{\mathrm{i}}}\left(\frac{\partial^{2}\overline{\varphi}_{\mathrm{m}}}{\partial z^{2}}+\frac{\partial^{2}\overline{\varphi}_{\mathrm{e}}^{'}}{\partial z^{2}}\right).$$

(16)

The equation reduces to the conventional CE when only considering a linear membrane with conductance independent of φ_{m}. Taking $\bar{\varphi}_{\mathrm{m}}$ again as the reduced potential together with $\mathscr{E}^{\mathrm{L}} = V_{\mathrm{r}}$ and $g_{\mathrm{m}}^{\mathrm{L}}=r_{\mathrm{m}}^{-1}$, (16) can be rearranged into the conventional form

$$\tau_{\mathrm{m}}\frac{\partial\overline{\varphi}_{\mathrm{m}}}{\partial t}+\overline{\varphi}_{\mathrm{m}}-\lambda^{2}\frac{\partial^{2}\overline{\varphi}_{\mathrm{m}}}{\partial z^{2}}=\lambda^{2}\frac{\partial^{2}\overline{\varphi}_{\mathrm{e}}^{'}}{\partial z^{2}}\triangleq f(z,t),\quad(17)$$

with time constant $\tau_{\mathrm{m}} = r_{\mathrm{m}}c_{\mathrm{m}}$, length constant $\lambda^2 = R_{\mathrm{m}}/R_{\mathrm{i}}$, and membrane resistance per unit length $R_{\mathrm{m}} = r_{\mathrm{m}}/(2\pi R)$. The activating function f should be interpreted in terms of the normalization condition (9), as the average of the (primary) extracellular potential around the neural compartment. Hence, the CE is accurate in terms of describing the average membrane potential at any axial position for small disturbances [20].

When nonlinear ion channels are considered, although the driving term is symmetric with regard to $\bar{\varphi}_{\mathrm{m}} - \mathscr{E}^{(j)}$, the membrane conductance around the circumference can be highly asymmetric due to the nonlinear voltage dependence of channel conductance. In general, for an axonal compartment of length L

$$I_{\mathrm{ion}}^{(j)}=L\cdot 2R\int_{0}^{\pi}g_{\mathrm{m}}^{(j)}(\varphi_{\mathrm{m}}(\theta))\cdot(\varphi_{\mathrm{m}}(\theta)-\mathscr{E}^{(j)})\cdot\mathrm{d}\theta\neq 2\pi\mathrm{RL}\cdot g_{\mathrm{m}}^{(j)}(\overline{\varphi}_{\mathrm{m}})\cdot(\overline{\varphi}_{\mathrm{m}}-\mathscr{E}^{(j)}).\quad(18)$$

Therefore, even if the average membrane potential $\bar{\varphi}_{\mathrm{m}}$ is close to rest, the imbalance of current densities on opposite sides of the membrane may depolarize the axon segment sufficiently to produce transverse activation.

For the soma, the ionic current of the compartment can be determined similarly by setting the dimension parameter n_{D} to 2 in (8) and integrating over the surface

$$I_{\mathrm{ion}}^{(j)}=2\pi R^{2}\int_{0}^{\pi}g_{\mathrm{m}}^{(j)}\left(\overline{\varphi}_{\mathrm{m}}+\frac{3}{2}E_{\mathrm{x}}^{'}R\cos\theta\right)\cdot\left(\overline{\varphi}_{\mathrm{m}}+\frac{3}{2}E_{\mathrm{x}}^{'}R\cos\theta-\mathscr{E}^{(j)}\right)\cdot\sin\theta\mathrm{d}\theta.\quad(19)$$

TP will influence the soma less than the axon for a given radius, as the ionic current is less affected due to the smaller amplification of the membrane potential and the inclusion of the $\sin\theta$ term in the integration. On the other hand, somas have larger radii than axons and the influence of TP for a given E-field strength might be more pronounced. Therefore, the

susceptibility to transverse stimulation cannot be directly compared between axons and somas without discussion of specific cases.

2.3. Numerical implementation

2.3.1. Coupling of extracellular electric field—The modified CE couples applied extracellular fields similarly to the conventional CE. The potentials, for example φ_{FEM} as obtained from an FEM simulation of the volume conductor, are applied by setting $\overline{\varphi}_{\mathrm{e}}^{'}=\varphi_{\mathrm{FEM}}$ and interpreted as the normalization condition for each compartment. The transverse field component is included as $E_{\mathrm{x}}^{'}=E_{\mathrm{FEM}}$ for soma and $E_{\mathrm{x}}^{'}=E_{\mathrm{FEM}}\sin\alpha_{E,z}$ for axons, in which $\alpha_{E,z}$ is the angle between the E-field and the axon's local orientation. The transverse field is applied to axons and spherical structures such as the soma and synaptic boutons, and may be excluded for dendrites due to their small radii and lower density of nonlinear ion channels.

The modified CE derived herein was based on unmyelinated axons and its application to myelinated axons should consider the discontinuities of the membrane and extracellular spatial properties between the myelin and the nodes of Ranvier. To account for the longitudinal modulation in the transmembrane potential akin to TP, the continuous partial differential equation form of the modified CE can be obtained by performing an additional asymptotic two-scale expansion in the spatial domain [8]. However, the continuous CE needs to be discretized for simulation and it is fairly common to use multiple compartments to simulate the internode [45], especially if the properties have more variation than just those between nodes and internodes [46]. Also, such asymptotic expansion results in a CE on the larger scale of internodal distance, i.e., on the order of hundreds of micrometers to a few millimeters. While appropriate for long and straight peripheral fibers, such spatial resolution is insufficient and not generalizable for realistic axon morphology. Therefore, the modified CE can be applied to myelinated axons numerically by using (18) on nodal compartments, whereas the myelin largely shields the internodal axon from the transverse field due its own TP.

2.3.2. Discretization of membrane—The ionic current term in the modified CE is an integral and has to be discretized for numerical implementation. Following regular segmentation techniques in the axial direction, such as the d_lambda ($d\lambda$) rule used in NEURON [47], each compartment's membrane is discretized into N patches by dividing the azimuthal/polar angle equally between 0 and π. An odd $N=2M+1$ is preferred to have one patch hold explicitly the mean membrane potential. The integral becomes a sum over the values taken at the mid points of each membrane patch with

$$\theta_b=\pi/2+b\pi/N, b=-M,\ldots,M \quad N,M\in\mathbb{Z}^+. \tag{20}$$

The discretization of the membrane should balance between computational cost and accuracy and may vary depending on the specific application and axial location. In general, a discretization into 10–20 patches (intervals $\Delta\theta$ in the range of 9°–18°) provides sufficient accuracy. Instead of directly summing the ionic currents [22], we propose two equivalent methods that are compatible with conventional CE solvers.

2.3.3. Approach using equivalent ion channels—The first approach calculates the equivalent membrane conductance and reversal potential for the original compartment. For axonal compartments, each ion channel j has

$$\overline{g}_{\mathrm{m}}^{(j)}=\frac{1}{N}\sum_{b=1}^{N}g_{\mathrm{m}}^{(j)}(\overline{\varphi}_{\mathrm{m}}+2E_{\mathrm{x}}^{'}R\cos\theta_b). \tag{21}$$

$$\overline{\mathscr{E}}^{(j)}\overline{g}_{\mathrm{m}}^{(j)}=\frac{1}{N}\sum_{b=1}^{N}(\mathscr{E}^{(j)}-2E_{\mathrm{x}}^{'}R\cos\theta_b)\cdot g_{\mathrm{m}}^{(j)}(\overline{\varphi}_{\mathrm{m}}+2E_{\mathrm{x}}^{'}R\cos\theta_b)$$

Similarly, the equivalent ion channel parameters for a spherical cell are calculated with the corresponding dimensional parameter and summation weights

$$\overline{g}_{\mathrm{m}}^{(j)}=\frac{\pi}{2N}\sum_{b=1}^{N}g_{\mathrm{m}}^{(j)}\left(\overline{\varphi}_{\mathrm{m}}+\frac{3}{2}E_{\mathrm{x}}^{'}R\cos\theta_b\right)\cdot\sin\theta_b. \tag{22}$$

$$\overline{\mathscr{E}}^{(j)}\overline{g}_{\mathrm{m}}^{(j)}=\frac{\pi}{2N}\sum_{b=1}^{N}(\mathscr{E}^{(j)}-\frac{3}{2}E_{\mathrm{x}}^{'}R\cos\theta_b)\cdot g_{\mathrm{m}}^{(j)}(\overline{\varphi}_{\mathrm{m}}+\frac{3}{2}E_{\mathrm{x}}^{'}R\cos\theta_b)\cdot\sin\theta_b$$

From here, conventional methods to solve the CE can be used. In this approach, no additional membrane potential needs to be stored for each patch as they can be calculated from the average potential by adding the cos θ-dependent transverse field. Additional computational cost mostly comes from the state-variables of the nonlinear ion channels, which must be stored for each of the N membrane patches and updated at every time step.

2.3.4. Approach using existing cable equation solvers—Using existing CE solvers, representation of TP for each neuronal compartment can be achieved by designing a multicompartment structure. The connections within the structure have negligible intracellular resistivity, thus approximating the condition of uniform intracellular potential within the original compartment. By specifying the extracellular potentials of the structure according to the cosine-dependent modulation, the solver's solution becomes equivalent to that of the modified CE. Such an approach was used previously to study the effect of transverse polarization of the soma on activation threshold of retinal ganglion cells [40]. In contrast to this approach, which replaces existing compartments and may require rebuilding parts of the neuron model, we propose a simpler implementation in NEURON that is applicable to both the soma and axon segments.

Each compartment subject to transverse field has additional compartments attached to form a spoke-hub structure (Figure 2), with the parameters of the new compartments (spokes) and modification to the original compartment (hub) specified in Table I. The hub holds the mean

membrane potential and retains the topological connections to other neuronal segments. Its axial resistance is specified as the original value for axonal compartments and set to a negligible value for soma. The spoke compartments represent the aforementioned membrane discretization with their extracellular potentials modulated from the mean value at the hub. With the odd discretization given by (20), the θ_b values of the $2M$ spoke compartments are symmetrically distributed with respect to the hub. The hub and spokes retain the original membrane properties (i.e., membrane capacitance, ion channels) and have surface areas set to a fraction of the original value, each scaled by weights given in (21) or (22).

The computational cost in the spatial domain increases by a factor of $2M$ for all compartments subject to TP. Given the aforementioned discretization, the modified structure is at most one order of magnitude more complex than the original model and is significantly less complex than the dense meshing of a FEM. The temporal resolution and tree-like topology of the neuron model are both preserved, allowing efficient solution [48] with run-time complexity scaling linearly with the number of additional compartments.

3. Implementation and validation of the modified cable equation

3.1. Single compartment

We evaluated both implementations of the modified CE described in section 2.3 by studying the strength–duration curve of transverse stimulation of single compartment models. The classic Hodgkin-Huxley (HH) model [43], adjusted to room temperature (23.5°C) with Q_{10} = 3, was used, and cylindrical and spherical geometries were compared. The membrane capacitance was 1 μF/cm^2 and membrane specific resistance at rest was 1.48 kΩ·cm^2. Ion channel parameters are given in Appendix II. Various radii were examined in the range of 0.25–16 μm. Since the E-field threshold was inversely proportional to the radius for single compartments, the results were normalized and reported in terms of the product of the field strength and radius. A custom backward Euler solver was built in MATLAB (R2015a, The Mathworks, Inc., Natick, MA, USA) for the equivalent channel implementation, and NEURON was used to demonstrate the approach using an existing CE solver. The discretization of the membrane was set to N=15 ($\Delta\theta$=12°), and the simulation time step was set to 2 μs or adjusted for pulse durations shorter than or not a multiple of 2 μs. A binary search algorithm was used to find the action potential threshold with relative accuracy of 0.1%.

The strength–duration curves of single compartments are shown in Figure 3. As predicted in the analysis, normalized thresholds were higher for the spherical geometry. For short pulse durations, the curves deviate from the classical formula [49]

$$\Theta = \frac{\Theta_{\mathrm{rh}}}{1 - \mathrm{e}^{-\mathrm{PW}/\tau_{\mathrm{m}}}}, \quad (23)$$

where Θ and Θ_{rh} are the threshold stimulus amplitude and rheobase, respectively, and τ_{m} is the membrane time constant. Unlike the log–log slope of −1 in Lapicque's integrate-and-fire model, the slope of −0.79 agrees with a previous report of sodium-dominated activation by

transverse field [22]. The thresholds for different radii are identical within cell type and simulation method, and the results agree between the two implementation methods, with the CE solver yielding slightly lower thresholds. The discrepancy is smallest for long pulses (1%–5%) and is larger for shorter pulses (~ 10% for pulses of less than 5 μs duration). This is most likely because the CE solver method only approximates the condition of uniform intracellular potential and therefore is limited in accuracy for computation and representation of the modified CE.

3.2. Distributed cable

The modified CE was derived on the assumption that the TP under a uniform field approximates the effects of an arbitrary field distribution on any compartment in a distributed neural cable. Although the asymptotic model [20] demonstrated the theoretical validity of decoupling the longitudinal and transverse components, we tested this assumption numerically against analytical solutions over a wide range of parameters after extending the single compartment implementation to a distributed cable [48]. Specifically, the axon and point source model [26,28] was used, in which a point source cathode depolarizes the membrane of a nearby unmyelinated axon with rectangular pulses of varying duration.

The parameters from the single compartment model were used, with additional parameters for the axon and point source model given in Table II. The passive electrical parameters were adopted from a series of models [3,26,28,43] and the radius was set according to the two studies using linear models [26,28], corresponding to a $\tau_{TP} = 40.6$ ns. The large parameter space of axon–electrode distances H and pulse widths PW [28] was sampled logarithmically with 6 values per decade. The shortest pulse duration of 0.1 μs is $2.5 \cdot \tau_{TP}$, allowing TP to reach at least 90% of its steady state value. We extended our custom CE solver from a single compartment to cables with linear topology. The E-field was calculated for a point source [1] and coupled to the axon as described in section 2.3 (Figure 5, bottom left). The axon length in either direction was set to the larger of either $5 \cdot \lambda_{DC}$ (the cable's dc length constant) or $10 \cdot H$. The length of axon compartments was set to 82.1 μm using the $d\lambda$ rule [47] with $d\lambda = 0.1$, or shortened to one tenth of H for very close electrode placements. The simulation time step was set to the pulse duration for pulses shorter than 1 μs and to 1 μs for longer pulses.

To quantify the effect of TP, the maximum transmembrane potential was compared between the conventional and modified CE, with the percentage change,

$$\delta_{\varphi} = \frac{\max\limits_{z} \overline{\varphi}_{m} - \max\limits_{z,\theta} \varphi_{m}}{\max\limits_{z,\theta} \varphi_{m}} \times 100\%, \quad (24)$$

shown in Figure 4. This metric reflects the behavior of the central compartment closest to the electrode ($z = 0$) as the maximum depolarization always occurs there and is on the cathodal side ($\theta = 0$) when TP is included. The conventional CE consistently underestimated the maximum membrane depolarization. The influence of TP ranged from minimal, for long pulse durations and intermediate axon–electrode distances, to substantial, for short pulse

durations and very close or distant electrode placements. The results agree with analytical solutions [28] and a close comparison reveals errors only for axon–electrode distances less than 30 μm (left shaded regions, Figure 4) and greater than 10 mm. Although the decoupling of the longitudinal and transverse components is still valid, the assumption of a uniform transverse field breaks down for short distances. This breakdown occurs within a distance about one order of magnitude larger than the axon radius, which agrees with previous TP results for spherical cells showing a distance–radius ratio of 13 or more for a point source to have less than 10% error compared to a uniform field [25]. For most applications of neural stimulation (center shade region, Figure 4), the distance between electrodes and their neural targets is larger than this critical value, either due to the choice of electrode placement or tissue encapsulation [50–52]. On the other hand, the assumption behind the derivation of the modified CE is indeed valid for larger distances, and the source of error include the limited numerical accuracy of the analytical solution due to the truncation of spatial frequencies [28], as our results matched the steady state solution obtained with higher numerical accuracy [26] (details not shown). Although the relative change of the maximum membrane potential is greater at larger axon–electrode distances when TP is considered, the absolute magnitudes of depolarization are very small and neural activation at such distances is unlikely (see section 4.3). Therefore, neither of the two regions of error are of practical concern, and the assumptions of the modified CE are valid for most applications.

4. Effect of transverse polarization on neural activation threshold

For both analytical solutions and FEM-based methods, the effect of TP has been studied using linear membrane models. The maximum membrane polarization can be greatly affected if TP is considered and such changes are expected to affect stimulation threshold [26,28,38]. However, whether linear results translate to nonlinear membrane models has not been directly studied. We therefore apply our modified CE to several common scenarios in neural stimulation (Figure 5) and determined the effect of TP on activation threshold for two nonlinear membrane models.

4.1. Membrane models and simulation setup

The HH model was used for unmyelinated axons (see sections 3.1 and 3.2 and Appendix II for parameters). Although the channel properties correspond to much larger invertebrate axons (> 100 μm radius), we used a radius of 3 μm to compare changes in threshold to changes in polarization in the linear model. For unmyelinated axons, the coupling strength of the axial field depends on λ^2 and scales with the radius. Axial discretization for the HH model followed the dλ rule unless otherwise specified.

The single-cable Richardson-McIntyre-Grill (RMG) model [44], based on human peripheral nerve fibers [53] at body temperature (37°C), was chosen to represent myelinated axons. The axon parameters are shown in Table III. The nodal compartments contain fast sodium channels (m^3h), persistent sodium channels (p^3), and slow potassium channels (s). The channel conductances are given in Appendix II. Ten compartments were used to model each passive internode, which also had 3 μm radius (corresponding to 10 μm fiber diameter including the myelin). Myelin membrane properties were calculated for 120 myelin lamella.

Myelination increases the effective length constant by one to two orders of magnitude and therefore yielded stronger coupling between the axon and the axial field [8]. On the other hand, the coupling of the transverse field is significantly reduced as the internodes are mostly passive and shielded from the transverse field by the TP of myelin lamella.

The CE solver from section 3.2 was adapted to include the nonlinear ion channels and myelination. E-field distributions were obtained analytically and decomposed into axial and transverse components to solve the modified CE as described in section 2.3. Monophasic rectangular waveforms were applied with pulse durations between 1 μs and 10 ms (6 values per decade). Except for studying axon terminal activation, the activating function was manually forced to zero at terminals to prevent action potential generation there. Simulation time steps ranged between 2 to 5 μs and thresholds were determined within 0.5% accuracy.

To quantify the effect of TP on activation thresholds, the percentage difference of thresholds comparing the modified CE to the conventional CE was used

$$\delta_{\Theta}=\frac{\Theta_{\mathrm{MCE}}-\Theta_{\mathrm{CE}}}{\Theta_{\mathrm{CE}}}\times 100\%. \quad (25)$$

Θ_{MCE} and Θ_{CE} are respectively the thresholds of the modified and conventional CE, given in the appropriate form for the stimulation, e.g., E-field strength or electrode current. For most cases, the conventional and modified CE resulted in qualitatively similar threshold distributions; therefore, only results for the modified CE and their percentage difference compared to the conventional CE are presented. Results of the conventional CE are shown only when the distributions differed qualitatively.

4.2. Axon terminals and axon bends in uniform electric field

The activating term at axon terminals is proportional to the axial E-field strength, and therefore polarization and threshold are orientation-dependent [11,54,55]. Terminals are also more sensitive to the exogenous field, with each mV/mm axial field yielding one to two orders of magnitude larger polarization than each mV/mm^2 of activating function. We examined the effect of TP on the threshold for field orientations α between 0° and 90° (Figure 5, top left) with denser sampling for angles close to 90°. The axon lengths were 1 cm for the HH model (approximately $12.5\cdot\lambda_{\mathrm{DC}}$) and 4.6 cm for the RMG model (41 nodes and 40 internodes). The threshold was determined by an action potential ($\bar{\varphi}_{\mathrm{m}} \geq 0$) reaching the antidromic end, where the activating term was forced to zero. The RMG model was also tested with a synaptic bouton of 4.5 μm radius attached to the terminal node (Figure 5). For the spherical compartment, the entire field was considered transverse. Whereas realistic synapses have complex morphology and features such as a short section of demyelination in the pre-synaptic axon, this simplified geometry was intended to test the modified CE implementation with a mixed geometry.

The threshold was inversely proportional to the cosine of the field orientation, and TP had no observable effect on the threshold for most parameter combinations (Figure 6). Only when the field was nearly transverse ($\alpha > 85°$) did TP decrease threshold, especially for short

pulse durations. As expected, the effect of TP was minimal when myelination was considered. The addition of the presynaptic terminal increased threshold by an order of magnitude due to the much larger surface area at the terminal; however, the influence of TP was stronger over a wider range of field orientations because any orientation was transverse to the spherical terminal.

Curvature in either the axon or the field polarizes the membrane based on the activating function [11,56,57], and activation is expected for bends of white matter fibers as they leave or approach the gray matter. The effect of TP on threshold was examined for field orientations α between 0° and 135° (Figure 5, top right). Beyond 135°, the activating function was negative everywhere and only hyperpolarization occurred at the bend. The radius of the curvature was 0.5 mm for the HH model, and the curved section was about one λ_{DC} long. The RMG model had a bend radius of 3 mm, and the curved section had length spanning 4 internodes. The curve was flanked by straight sections of 20 mm lengths on both sides. Threshold was determined at the center of the straight section and was analyzed for both orthodromic (shown as arrow in figure) and antidromic propagation.

In the HH model (Figure 7, left column), thresholds were identical (within 1%) for orthodromic and antidromic propagation for field orientations pointing into (0°–45°) or inward tangent (45°–90°, field is more aligned with the straight segment proximal to the bend than distal) to the bend, and TP did not affect threshold (parameter space left to gray and white dashed line). As the field orientation turned outward tangent to the bend (> 90°, field is more aligned with distal axon), orthodromic activation exhibited lower thresholds for long pulse durations (between gray and white dashed lines). With the conventional CE, orthodromic activation remained the only mechanism of activation (between white dashed and solid lines, 95°–115°) before hyperpolarization prevented action potential generation beyond a certain orientation ($\alpha_2 \approx 115°$, right of white solid line). For the modified CE, in comparison, TP in the proximal axon decreased threshold for outward tangent field orientations (95°–115°) and allowed transverse activation with lower antidromic thresholds ($\alpha_1 \approx 105°–110°$, right to white dashed line).

The RMG model (Figure 7, right column) had lower thresholds overall and similar behaviors for field orientations into or inward tangent to the bend. There was also orthodromic preferred activation for outward tangent orientations and long pulse durations (between gray dashed line and white lines). For the conventional CE, however, hyperpolarization only prevented action potentials for short pulse durations ($\alpha_2 \approx 110°–115°$, within white solid line) and anode-break excitation occurred for longer pulses (white dotted line); for the modified CE, TP resulted in transverse activation for short pulse durations ($\alpha_1 \approx 110°–115°$, white dashed line) and anode-break excitation occurred for longer pulses (white dotted line). The effect of TP on threshold was limited to a very small parameter space.

Overall, transverse polarization influences threshold for some field orientations in the HH model and has minimal effect in the RMG model. The modified CE is valid for curved axons when the radius of curvature is larger than the axon radius and similar to the length constant. Results varied quantitatively based on the ratio between the bend radius and the length constant; however, qualitative feature were persistent with shifts for the boundaries (α_1 and

a_2) of the different behavior. A more gradual curvature allowed the conventional activating function to produce activation over a wider orientation angles (larger a_2), whereas tighter bends led to the opposite, i.e., larger parameters space of transverse activation due to TP (smaller a_1).

4.3. Axonal stimulation by point source and disk electrodes

Point sources (Figure 5, bottom left) are often used to model stimulating electrodes. The thresholds of the nonlinear models were examined within a smaller and more representative parameter space compared to the linear model in section 3.2. The axon–electrode distance H ranged between 30 μm and 3 cm, sampled with 6 values per decade. Minimal axon length was at least $5H$ or 8.0 mm ($10{\cdot}\lambda_{DC}$) in either direction; the dλ rule or a maximum of H/5 was used for axial discretization of the HH model. For the RMG model, the electrode was aligned with the central node to maximize the transverse field and the effect of TP. Threshold was determined as action potentials reaching axial locations at least 2 mm or $3H$ away from the center in either direction. This distance allowed propagation beyond the point of maximum hyperpolarization at $\pm\sqrt{3/2}H$.

Disk electrodes (Figure 5, bottom right) are commonly used to represent larger flat electrodes used in stimulation applications. The radius of the disk electrode was 100 μm and the analytical steady state solution of an ideal disk electrode in a semi-infinite medium [58,59] was used for all pulse widths. The axon was positioned parallel to the electrode surface and aligned through its center. All other parameters were the same as the point source electrodes.

The thresholds of the HH model (Figure 8) exhibited behaviors consistent with literature for both point source and disk electrodes, including the −1 log–log slope of the strength–duration curve and the quadratic relationship between threshold current and electrode distance [44]. Threshold currents were smaller for the disk electrode due to the insulating substrate "doubling" the effective current amplitude compared to the point source. The near field ($H \leq 100$ μm) behavior differed slightly between the two electrodes, with smaller thresholds for the point source (adjusted for the doubling). TP affected thresholds only for large electrode distances ($H > 10$ mm) and short pulse durations; however, thresholds for such parameters were unrealistically high (even considering the use of the HH model with a small axon radius).

The influence of TP on thresholds in the nonlinear models can be compared against its influence on membrane polarization in the linear axon membrane model (section 3.2). For a linear membrane, thresholds can be estimated from the maximum depolarization, in which action potentials are triggered whenever the membrane depolarizes to a certain voltage threshold. Therefore, the stimulus amplitude threshold of the linear membrane model is inversely proportional to the maximum membrane depolarization for a given pulse width and electrode distance, i.e., $\hat{\Theta} \propto (\max \varphi_m)^{-1}$, and the percentage change of the predicted threshold $\delta_{\hat{\Theta}}$ is equal to the percentage change of the maximum depolarization δ_{φ}. Figure 8 shows that the results with a nonlinear membrane do not agree with those of the linear membrane model. The predictions with the linear membrane fail because they attempt to

account for the behavior of an entire cylindrical compartment (the center compartment where both the activating function and transverse field are strongest) based on an infinitesimal thin slice of its membrane (single point in the case of spherical geometry). In contrast, the nonlinear membrane model captures the behavior of the entire compartment using the modified CE. The polarity of membrane polarization around the center compartment does not change for most parameters (50% dashed contour line), and even for large electrode distances and short pulse durations, only a relatively small fraction of the membrane on the anodal side reverses polarity to hyperpolarization. The behavior of the ion channels is dominated by the average potential of the compartment. Nonlinearities are small second-order functions of cos θ and the first-order function of TP is averaged out when the ionic currents are integrated over the entire surface. Transverse-field dominated activation only occurs when $\bar{\varphi}_m$ is close to rest and the average depolarization is negligible compared to TP, allowing the two sides of the membrane to polarize with opposite polarity.

For the RMG model, the behavior (threshold, chronaxie, current–distance curves, etc.) agreed with the original model [44] and the distribution of thresholds was qualitatively similar to the HH model but with smaller amplitude (Figure 9). However, the modified CE revealed that TP caused less than 2% reductions in threshold over the same parameter space.

5. Discussion

5.1. Transverse polarization and modified cable equation

TP is a fundamental response of neuronal elements to exogenous E-fields and provides a sound biophysical foundation to describe quantitatively the coupling between extracellular E-fields and excitable cells. The modified CE captures the effects of TP by modeling the full 3-D geometry and secondary fields generated by the membrane, thereby addressing limitations of the conventional CE. The modified CE reduces to the conventional form for a linear membrane, revealing that the latter is an accurate description of the average membrane polarization for subthreshold responses to exogenous E-fields. The analysis also demonstrates that the presence of the neuron does not affect the normalization condition based on extracellular fields (see equations (7) and (9)). Therefore, the secondary field generated by the presence of the neuron can be ignored for both the conventional and modified CE when calculating the activating function, which is defined based on the relationship of the normalization in the axial direction (9).

We demonstrated two implementations of the modified CE, both without significant adjustment to current algorithms or solvers. This compatibility reduces computational cost and complexity, allowing flexible inclusion of TP in simulations. As TP only occurs when exogenous fields are present, a further improvement is to switch the simulation from conventional to the modified CE when a transverse field is applied and back when TP modulation of the ion channels diminishes and all the membrane patches converge to the compartment's average. The computational overhead for such switching is justified if the interpulse intervals are significantly longer than the pulse duration, as is typically the case.

5.2. Thresholds from linear versus nonlinear membrane models

Linear membrane models were used previously to estimate the effects of TP on membrane polarization, with the assumption that the neural activation threshold is inversely proportional to the maximum depolarization around the membrane circumference. This assumption is equivalent to an idealized, fixed voltage threshold for action potential generation applied to all membrane positions. This linear model predicted substantial effects of TP on activation thresholds. However, using the modified CE and several stimulation configurations with nonlinear membrane models, we demonstrated that the effect of TP on the activation threshold is much smaller than expected from the linear models and can be neglected for most applications. This discrepancy demonstrates that the fixed threshold assumption, when applied to each point around the circumference of the membrane, introduces an unrealistically strong nonlinear amplification mechanism that does not comport with the softer nonlinearity of a realistic membrane and therefore significantly overestimates the effect of TP on activation thresholds.

Despite allowing transverse activation in some of the simulated scenarios, in most realistic situations TP is unlikely to affect thresholds at axon terminals or bends. The relatively symmetric distribution of dendrites and axon collaterals, for example of cortical neurons, results in low threshold activation of aligned terminals or bends before TP can activate transverse branches at much higher field strength. For axons, the threshold changes due to TP are insignificant for typical electrode and current parameters (pulse duration > 10 μs and electrode distance < 1 cm), especially for myelinated axons. Large electrode distances are only present in transcranial electrical stimulation, for which the model's assumption of straight and sufficiently long axons is invalid.

Several other factors not included in our simulations are unlikely to change the conclusion that the effect of TP is minimal. When branching of the neural cable is considered, for example in dendritic arbors, additional terms are introduced into the CE at branch points to balance the axial currents. These terms are determined by the longitudinal field components and result in stronger activating functions compared to unbranched cables. Similarly, changes and especially discontinuities in parameters along the cable for example changes in diameter, also increase the activating function term. Furthermore, the interaction between neighboring fibers shields the applied field and reduces the TP of each axon. The effect is strongly dependent on the density of the cell packing, and may significantly reduce or even eliminate the $1/n_D$ factor in the TP solution [34–36,38]. Therefore, realistic threshold changes due to TP are even smaller, and the percentage changes obtained in our study are an upper boundary. Overall, the conventional CE captures the neuronal response with accuracy sufficient for most practical applications of electrical stimulation.

5.3. Potential significance of modified cable equation

Despite the limited effect of TP on axonal activation thresholds, the modified CE could be used to explore specific stimulation scenarios where TP may be significant. For example, simulations could routinely include TP for the soma due to its size and proximity to the highly sensitive axon initial segment [40]. Further, models of magnetic stimulation could potentially benefit from the modified CE because the short pulse duration and low spatial

gradient of the induced E-field are characteristics associated with relatively strong influence of the transverse field. Moreover, subthreshold modulation due to TP could be of interest for modeling of network level behavior. Finally, ephaptic coupling between neighboring neural elements can also be studied without building FEM [39]. A neural element with significant membrane current $I_{\mathrm{m}}(t)=\int i_{\mathrm{m}}(t)\mathrm{d}S$ during action potentials generates an additional extracellular field that can be approximated by a series of time-dependent point sources, each representing a compartment of the neural membrane. At a neighboring compartment, the resulting field is added to existing extracellular fields and then applied to the modified CE. Such contributions are needed for only a limited number of predetermined neural elements that satisfy certain conditions, such as short separation distances and large ionic currents at the source element.

5.4. Limitations

Although the CE modified with TP improves the conventional CE significantly, it is still an approximation to the actual field distribution due to interaction of cell membranes with applied or self-generated E-field, especially for complex neural microstructures. For example, the branching of axons or dendrites may result in strong interaction of the secondary fields arising from cable segments close to the branching point. The analysis did not consider ephaptic interactions between neighboring neurons or the influence of a confined extracellular space. Further, any change in axon radius along the axial direction was assumed to be small, while the radius can indeed vary, for example following branching or at the axon hillock. For the myelinated axons, the modified CE did not accurately represent detailed geometrical properties of the periaxonal space, myelin attachment, paranode, and node [46]. Also, the adjustment term for the soma was derived for an ideal spherical geometry, whereas realistic neurons have irregularly-shaped somas that are further complicated by the dendritic arbor [38]. A detailed comparison with morphologically faithful FEM can further evaluate how well the modified CE captures the neural behavior in such cases.

6. Conclusions

We developed a theoretical framework to include the contribution of TP to the spatiotemporal distribution of neuronal transmembrane potential as described with a modified CE. Two numerical methods were proposed for implementation of the modified CE in general as well as in specialized CE solvers. The implementations for single compartments and distributed axonal cables were validated, and the effect of TP on the activation threshold was quantified for several common neural stimulation scenarios using two nonlinear membrane models. TP had a minimal effect in most electrical stimulation applications and only affected threshold for unmyelinated axons when the applied field had very short pulse durations and low spatial gradient. These results indicate that previously published models of TP using linear membrane models significantly overestimated the effect of TP on activation thresholds. The modified CE provides a full and coherent theory that addresses the limitations of these earlier TP models as well as of the conventional CE. The small effect of TP demonstrated for typical scenarios with the modified CE helps to validate the assumptions and approximations of the conventional CE. When necessary or desired, the

modified CE provides a simple solution to include TP for nonlinear membranes without involving complex and computationally expensive FEMs.

Acknowledgments

This work was supported by Grant No. R01NS088674 from the National Institutes of Health and a Research Grant by Tal Medical. The simulations in this work utilized the Duke Compute Cluster. The authors would like to thank Dr. Wanda K. Neu for comments on the manuscript, Dr. Stefan M. Goetz for discussion of electromagnetic–neuronal coupling, and Dr. N. Ted Carnevale for suggestions on the NEURON simulations. Preliminary results of this study were presented at the Joint Meeting of the North American Neuromodulation Society and the Neural Interfaces Conference (NANS^2-NIC, June 2016, Baltimore, MD, USA) and the 6th International Conference on Transcranial Brain Stimulation (September 2016, Göttingen, Germany) [60].

List of symbols and notation

x, y, z	Cartesian coordinates
ρ, θ, z	Cylindrical coordinates: radial, azimuthal, and axial coordinate
ρ, θ, ϕ	Spherical coordinates: radial, polar, and azimuthal coordinate
n_{D}	Dimension parameter
$\hat{x}, \hat{\rho}$	Unit vectors
$\varphi, \varphi', \varphi''$	Electrical potentials: total field, primary/applied field, and secondary/response field
$\vec{E}, E_{\mathrm{x}}$	Electric field: vector and component
$\sigma_{\mathrm{i,e}}$	Intra- and extracellular conductivities
R	Radius of axon or soma
L	Length of axonal compartment
S	Surface area of neural compartment
$\varphi_{\mathrm{m}}, i_{\mathrm{m}}$	Transmembrane potential and current density
$c_{\mathrm{m}}, r_{\mathrm{m}}$	Specific membrane capacitance and resistance
$\tau_{\mathrm{m}}, \tau_{\mathrm{c}}, \tau_{\mathrm{TP}}$	Time constant of membrane, cell, and transverse polarization
$g_{\mathrm{m}}^{(j)}, \mathscr{E}^{(j)}$	Conductance and reversal potential for ion channel j
$I_{\mathrm{i}}, R_{\mathrm{i}}$	Axon's axial current and axial resistance per unit length
R_{m}	Axon's membrane resistance per unit length
λ	Axon's length constant

f	Activating function
Θ	Threshold
δ	Percentage change

Appendix I

Solution of transverse polarization in cylindrical and spherical cells

The potential of the applied primary field has the form $\varphi' = -E'_{\mathrm{x}}\rho\cos\theta$ in the cylindrical/spherical coordinate system when assuming the neuron is absent. The potential of the secondary field has a similar form $\varphi'' = E'_{\mathrm{x}}P(\rho)\cos\theta$. Considering cylindrical and spherical harmonics with natural boundary conditions so that $P(\rho)$ is bounded and $P(\infty) = 0$, Laplace's equation (2) yields

$$\begin{cases} \varphi''_{\mathrm{i}} = -E'_{\mathrm{x}}\rho\cos\theta\cdot A(t) \\ \varphi''_{\mathrm{e}} = -E'_{\mathrm{x}}\rho^{-n_{\mathrm{D}}}\cos\theta\cdot B(t) \end{cases}. \quad (26)$$

Two more time constants are introduced besides τ_{m}. The cellular time constant τ_{c} is

$$\tau_{\mathrm{c}} = \mathrm{Rc}_{\mathrm{m}}\left(\frac{1}{\sigma_{\mathrm{i}}} + \frac{1}{n_{\mathrm{D}}\sigma_{\mathrm{e}}}\right), \quad (27)$$

which is the time constant of charge redistribution on the cell membrane. The transverse polarization time constant τ_{TP} combines the contribution of both τ_{c} and τ_{m}

$$\tau_{\mathrm{TP}}^{-1} = \tau_{\mathrm{m}}^{-1} + \tau_{\mathrm{c}}^{-1}. \quad (28)$$

The full temporal solution to the system of equations is [4,21]

$$\varphi''_{\mathrm{i}} = E'_{\mathrm{x}}\rho\cos\theta\left\{1 - \frac{(n_{\mathrm{D}}+1)\sigma_{\mathrm{e}}}{n_{\mathrm{D}}\sigma_{\mathrm{e}}+\sigma_{\mathrm{i}}}[\mathrm{e}^{-t/\tau_{\mathrm{TP}}} + (1-\mathrm{e}^{-t/\tau_{\mathrm{TP}}})\epsilon]\right\}. \quad (29)$$

$$\varphi''_{\mathrm{e}} = -\frac{E'_{\mathrm{x}}R^{n_{\mathrm{D}}+1}}{n_{\mathrm{D}}\rho^{n_{\mathrm{D}}}}\cos\theta\left\{1 - \frac{(n_{\mathrm{D}}+1)\sigma_{\mathrm{i}}}{n_{\mathrm{D}}\sigma_{\mathrm{e}}+\sigma_{\mathrm{i}}}[\mathrm{e}^{-t/\tau_{\mathrm{TP}}} + (1-\mathrm{e}^{-t/\tau_{\mathrm{TP}}})\epsilon]\right\}$$

where $\epsilon = \tau_{\mathrm{TP}}/\tau_{\mathrm{m}}$. The solution contains two transients, namely TP via global charge redistribution and local membrane charging. The membrane polarization is

$$\varphi_{\mathrm{m}}=E_{\mathrm{x}}^{'}R\cos\theta(1+1/n_{\mathrm{D}})(1-\mathrm{e}^{-t/\tau_{\mathrm{TP}}})(1-\epsilon). \quad (30)$$

If the intra- and extra-cellular spaces have different conductivities, there is also a net charge density q_s stored on the membrane

$$q_{\mathrm{s}}=E_{\mathrm{x}}^{'}\cos\theta\frac{(n_{\mathrm{D}}+1)(\sigma_{\mathrm{i}}\mathscr{E}_{\mathrm{e}}-\sigma_{\mathrm{e}}\mathscr{E}_{\mathrm{i}})}{n_{\mathrm{D}}\sigma_{\mathrm{e}}+\sigma_{\mathrm{i}}}\left[\mathrm{e}^{-t/\tau_{\mathrm{TP}}}+(1-\mathrm{e}^{-t/\tau_{\mathrm{TP}}})\epsilon\right]. \quad (31)$$

where $\mathscr{E}_{\mathrm{i,e}}$ are the permittivity of the intra- and extra-cellular spaces.

Given typical values for conductivities of 1–10 mS/cm, membrane capacitance of 1 μF/cm^2, and radius of 1–10 μm, the cellular time constant is in the range of 10–100 ns, with the lower and upper bounds corresponding to axons and somas, respectively. With $\sigma_{\mathrm{m}} \ll \sigma_{\mathrm{i,e}}$ and membrane resistance of 1–10 kΩ·cm^2, the typical membrane time constant at rest is much larger (1–10 ms). Therefore, $\tau_{\mathrm{TP}} \approx \tau_{\mathrm{c}} < 1$ μs and $\epsilon \approx 10^{-5}$–10^{-4}. Under this approximation, the potentials at steady state after TP are given in (8) by setting the exponential decays to zero and substituting (27) and (28) in (29) and (30). Figure 10 illustrates the steady state with the charge distribution shown on the membrane.

When an E-field with full 3-D variation is applied to an axon, the solution for Laplace's equation is in the form of cylindrical harmonics $(A_m(k)I_m(k\rho) + B_m(k)K_m(k\rho))$ exp jkz exp j$m\theta$ [26,28,30,31,35,36], where $I_m(k\rho)$ and $K_m(k\rho)$ are m^{th}-order modified Bessel functions of the first and second kinds, respectively. The parameters k and m describe spatial variation of the field in the axial and azimuthal directions. For the azimuthal parameter, the zeroth mode is the longitudinal solution of CE with axial symmetry. Non-zero modes correspond to transverse solutions whose amplitude is modulated by the spatial frequency along the axis. The secondary field generated by neurons during TP does not affect the local normalization condition (7) due to the cos $m\theta$-modulation for any transverse modes. The first mode corresponds to uniform transverse field, and higher modes represent multipolar transverse field distributions. It is highly unlike that any realistic applications have microscopic multipolar field distribution, and therefore $m \geq 2$ terms typically have much smaller amplitude; the first order term dominates the transverse field, and high order terms can be safely neglected [35]. Due to the slow changes of the field in the axial direction, the spatial frequency k of the applied field is very small, typically on the order of 0.1–1 mm^{-1}. Therefore $k\rho \ll 1$ holds for ρ on the cellular scale of micrometers and the potentials degenerate into the same form as (26) under the approximations $I_1(k\rho) \propto \rho$ and $K_1(k\rho) \propto \rho^{-1}$. Hence the solution of TP under uniform E-field condition can be used for most realistic exogenous field distributions.

Appendix II

Ion channel conductance and dynamics

The original HH model [43] is used at room temperature. The RMG model [44] contains HH-type fast sodium channels (m^3h), persistent sodium channels (p^3), and slow potassium channels (s) at the nodes of Ranvier. The parameters of both models are listed in Table IV. For channel dynamics and their temperature dependence, please refer to the original publications.

References

1. McNeal DR. Analysis of a Model for Excitation of Myelinated Nerve. IEEE Trans. Biomed. Eng. 1976; BME-23:329–37.
2. Rattay F. Analysis of Models for External Stimulation of Axons. IEEE Trans. Biomed. Eng. 1986; BME-33:974–7.
3. Roth BJ, Basser PJ. A model of the stimulation of a nerve fiber by electromagnetic induction. IEEE Trans. Biomed. Eng. 1990; 37:588–97. [PubMed: 2354840]
4. Cartee LA, Plonsey R. The transient subthreshold response of spherical and cylindrical cell models to extracellular stimulation. IEEE Trans. Biomed. Eng. 1992; 39:76–85. [PubMed: 1572684]
5. Warman EN, Grill WM, Durand D. Modeling the effects of electric fields on nerve fibers: Determination of excitation thresholds. IEEE Trans. Biomed. Eng. 1992; 39:1244–54. [PubMed: 1487287]
6. Nagarajan SS, Durand DM. A generalized cable equation for magnetic stimulation of axons. IEEE Trans. Biomed. Eng. 1996; 43:304–12. [PubMed: 8682543]
7. Ruohonen J, Panizza M, Nilsson J, Ravazzani P, Grandori F, Tognola G. Transverse-field activation mechanism in magnetic stimulation of peripheral nerves. Electroencephalogr. Clin. Neurophysiol. Mot. Control. 1996; 101:167–74.
8. Basser PJ. Cable equation for a myelinated axon derived from its microstructure. Med. Biol. Eng. Comput. 1993; 31:S87–92. [PubMed: 8231331]
9. Ilmoniemi RJ, Mäki H, Saari J, Salvador R, Miranda PC. The Frequency-Dependent Neuronal Length Constant in Transcranial Magnetic Stimulation. Front. Cell. Neurosci. 2016; 10
10. Arlotti, M., Rahman, A., Minhas, P., Bikson, M. Axon terminal polarization induced by weak uniform DC electric fields: A modeling study; 2012 Annual International Conference of the IEEE Engineering in Medicine and Biology Society 2012 Annual International Conference of the IEEE Engineering in Medicine and Biology Society; 2012. p. 4575-8.
11. Silva S, Basser PJ, Miranda PC. Elucidating the mechanisms and loci of neuronal excitation by transcranial magnetic stimulation using a finite element model of a cortical sulcus. Clin. Neurophysiol. 2008; 119:2405–13. [PubMed: 18783986]
12. Joucla S, Glière A, Yvert B. Current approaches to model extracellular electrical neural microstimulation. Front. Comput. Neurosci. Front. Comput. Neurosci. 2014; 8:1–12. [PubMed: 24550816]
13. Wongsarnpigoon A, Grill WM. Computer-based model of epidural motor cortex stimulation: Effects of electrode position and geometry on activation of cortical neurons. Clin. Neurophysiol. 2012; 123:160–72. [PubMed: 21775202]
14. Wesselink WA, Holsheimer J, Boom HBK. A model of the electrical behaviour of myelinated sensory nerve fibres based on human data. Med. Biol. Eng. Comput. 1999; 37:228–35. [PubMed: 10396827]
15. Greenberg RJ, Velte TJ, Humayun MS, Scarlatis GN, de Juan E Jr. A computational model of electrical stimulation of the retinal ganglion cell. IEEE Trans. Biomed. Eng. 1999; 46:505–14. [PubMed: 10230129]

16. Smit JE, Hanekom T, Hanekom JJ. Predicting action potential characteristics of human auditory nerve fibres through modification of the Hodgkin-Huxley equations. South Afr. J. Sci. 2008; 104:284–92.
17. Rotem A, Moses E. Magnetic stimulation of curved nerves. IEEE Trans. Biomed. Eng. 2006; 53:414–20. [PubMed: 16532767]
18. Salvador R, Silva S, Basser PJ, Miranda PC. Determining which mechanisms lead to activation in the motor cortex: A modeling study of transcranial magnetic stimulation using realistic stimulus waveforms and sulcal geometry. Clin. Neurophysiol. 2011; 54(11):1719–1725.
19. Krassowska W, Neu JC. Response of a single cell to an external electric field. Biophys. J. 1994; 66:1768. [PubMed: 8075318]
20. Cranford JP, Kim BJ, Neu WK. Asymptotic model of electrical stimulation of nerve fibers. Med. Biol. Eng. Comput. 2012; 50:243–51. [PubMed: 22350436]
21. Ying W, Henriquez CS. Hybrid Finite Element Method for Describing the Electrical Response of Biological Cells to Applied Fields. IEEE Trans. Biomed. Eng. 2007; 54:611–20. [PubMed: 17405368]
22. Boinagrov D, Loudin J, Palanker D. Strength–Duration Relationship for Extracellular Neural Stimulation: Numerical and Analytical Models. J. Neurophysiol. 2010; 104:2236–48. [PubMed: 20702740]
23. Klee M, Plonsey R. Stimulation of Spheroidal Cells - The Role of Cell Shape. IEEE Trans. Biomed. Eng. 1976; BME-23:347–54.
24. Gimsa J, Wachner D. Analytical Description of the Transmembrane Voltage Induced on Arbitrarily Oriented Ellipsoidal and Cylindrical Cells. Biophys. J. 2001; 81:1888–96. [PubMed: 11566763]
25. Lee DC, Grill WM. Polarization of a Spherical Cell in a Nonuniform Extracellular Electric Field. Ann. Biomed. Eng. 2005; 33:603–15. [PubMed: 15981861]
26. Schnabel V, Struijk JJ. Evaluation of the cable model for electrical stimulation of unmyelinated nerve fibers. IEEE Trans. Biomed. Eng. 2001; 48:1027–33. [PubMed: 11534838]
27. Livshitz LM, Einziger PD, Mizrahi J. Rigorous Green's function formulation for transmembrane potential induced along a 3-D infinite cylindrical cell. IEEE Trans. Biomed. Eng. 2002; 49:1491–503. [PubMed: 12549731]
28. Neu WK. Analytical solution for time-dependent potentials in a fiber stimulated by an external electrode. Med. Biol. Eng. Comput. 2016:1–7.
29. Neu, WK. Uncertainty in 1D and 3D Models of a Fiber Stimulated by an External Electrode. In: Ortuño, F., Rojas, I., editors. Bioinformatics and Biomedical Engineering Lecture Notes in Computer Science. Springer International Publishing; 2016. p. 219-29.
30. Meffin H, Tahayori B, Grayden DB, Burkitt AN. Modeling extracellular electrical stimulation: I. Derivation and interpretation of neurite equations. J. Neural Eng. 2012; 9:065005. [PubMed: 23187045]
31. Tahayori B, Meffin H, Dokos S, Burkitt AN, Grayden DB. Modeling extracellular electrical stimulation: II. Computational validation and numerical results. J. Neural Eng. 2012; 9:065006. [PubMed: 23187093]
32. Ye H, Cotic M, Carlen PL. Transmembrane potential induced in a spherical cell model under low-frequency magnetic stimulation. J. Neural Eng. 2007; 4:283. [PubMed: 17873431]
33. Ye H, Cotic M, Fehlings MG, Carlen PL. Transmembrane potential generated by a magnetically induced transverse electric field in a cylindrical axonal model. Med. Biol. Eng. Comput. 2010; 49:107–19. [PubMed: 21063912]
34. Pavlin M, Pavselj N, Miklavcic D. Dependence of induced transmembrane potential on cell density, arrangement, and cell position inside a cell system. IEEE Trans. Biomed. Eng. 2002; 49:605–12. [PubMed: 12046706]
35. Meffin H, Tahayori B, Sergeev EN, Mareels IMY, Grayden DB, Burkitt AN. Modelling extracellular electrical stimulation: III. Derivation and interpretation of neural tissue equations. J. Neural Eng. 2014; 11:065004. [PubMed: 25419585]
36. Tahayori B, Meffin H, Sergeev EN, Mareels IMY, Burkitt AN, Grayden DB. Modelling extracellular electrical stimulation: IV. Effect of the cellular composition of neural tissue on its spatiotemporal filtering properties. J. Neural Eng. 2014; 11:065005. [PubMed: 25419652]

37. Voßen C, Eberhard JP, Wittum G. Modeling and simulation for three-dimensional signal propagation in passive dendrites. Comput. Vis. Sci. 2007; 10:107–21.
38. Agudelo-Toro A, Neef A. Computationally efficient simulation of electrical activity at cell membranes interacting with self-generated and externally imposed electric fields. J. Neural Eng. 2013; 10:026019. [PubMed: 23503026]
39. Xylouris K, Wittum G. A three-dimensional mathematical model for the signal propagation on a neuron's membrane. Front. Comput. Neurosci. 2015; 9
40. Sergeev, EN., Meffin, H., Tahayori, B., Grayden, DB., Burkitt, AN. Effect of soma polarization on electrical stimulation thresholds of retinal ganglion cells; 2013th International IEEE/EMBS Conference on Neural Engineering (NER) 2013 6th International IEEE/EMBS Conference on Neural Engineering (NER); 2013. p. 1135-8.
41. Carnevale, NT., Hines, ML. The NEURON book. Cambridge University Press; 2006.
42. Mainen ZF, Sejnowski TJ. Influence of dendritic structure on firing pattern in model neocortical neurons. Nature. 1996; 382:363–6. [PubMed: 8684467]
43. Hodgkin AL, Huxley AF. A quantitative description of membrane current and its application to conduction and excitation in nerve. J. Physiol. 1952; 117:500–44. [PubMed: 12991237]
44. Richardson AG, McIntyre CC, Grill WM. Modelling the effects of electric fields on nerve fibres: Influence of the myelin sheath. Med. Biol. Eng. Comput. 2000; 38:438–46. [PubMed: 10984943]
45. Cartee LA. Evaluation of a model of the cochlear neural membrane. II: Comparison of model and physiological measures of membrane properties measured in response to intrameatal electrical stimulation. Hear. Res. 2000; 146:153–66. [PubMed: 10913892]
46. McIntyre CC, Richardson AG, Grill WM. Modeling the Excitability of Mammalian Nerve Fibers: Influence of Afterpotentials on the Recovery Cycle. J. Neurophysiol. 2002; 87:995–1006. [PubMed: 11826063]
47. Hines ML, Carnevale NT. Neuron: A Tool for Neuroscientists. The Neuroscientist. 2001; 7:123–35. [PubMed: 11496923]
48. Hines M. Efficient computation of branched nerve equations. Int. J. Biomed. Comput. 1984; 15:69–76. [PubMed: 6698635]
49. Lapicque L. Recherches quantitatives sur l'excitation électrique des nerfs traitée comme une polarisation. J Physiol Pathol Gen. 1907; 9:620–635.
50. Grill WM, Mortimer JT. Electrical properties of implant encapsulation tissue. Ann. Biomed. Eng. 1994; 22:23–33. [PubMed: 8060024]
51. Polikov VS, Tresco PA, Reichert WM. Response of brain tissue to chronically implanted neural electrodes. J. Neurosci. Methods. 2005; 148:1–18. [PubMed: 16198003]
52. Szarowski DH, Andersen MD, Retterer S, Spence AJ, Isaacson M, Craighead HG, Turner JN, Shain W. Brain responses to micro-machined silicon devices. Brain Res. 2003; 983:23–35. [PubMed: 12914963]
53. Schwarz JR, Reid G, Bostock H. Action potentials and membrane currents in the human node of Ranvier. Pflügers Arch. Eur. J. Physio. 1995; 430:283–92. [PubMed: 7675638]
54. Fox PT, Narayana S, Tandon N, Sandoval H, Fox SP, Kochunov P, Lancaster JL. Column-based model of electric field excitation of cerebral cortex. Hum. Brain Mapp. 2004; 22:1–14. [PubMed: 15083522]
55. Rahman A, Reato D, Arlotti M, Gasca F, Datta A, Parra LC, Bikson M. Cellular effects of acute direct current stimulation: somatic and synaptic terminal effects. J. Physiol. 2013; 591:2563–78. [PubMed: 23478132]
56. Abdeen MA, Stuchly MA. Modeling of magnetic field stimulation of bent neurons. IEEE Trans. Biomed. Eng. 1994; 41:1092–5. [PubMed: 8001998]
57. Amassian VE, Eberle L, Maccabee PJ, Cracco RQ. Modelling magnetic coil excitation of human cerebral cortex with a peripheral nerve immersed in a brain-shaped volume conductor: the significance of fiber bending in excitation. Electroencephalogr. Clin. Neurophysiol. Potentials Sect. 1992; 8:291–301.
58. Newman J. Current Distribution on a Rotating Disk below the Limiting Current. J. Electrochem. Soc. 1966; 113:1235–41.

59. Wiley JD, Webster JG. Analysis and Control of the Current Distribution under Circular Dispersive Electrodes. IEEE Trans. Biomed. Eng. 1982; BME-29:381–5.

60. Wang B, Aberra AS, Grill WM, Peterchev AV. Incorporating initial polarization in neural simulations for accurate modeling of brain stimulation. Clin. Neurophysiol. 2017; 128:e52.

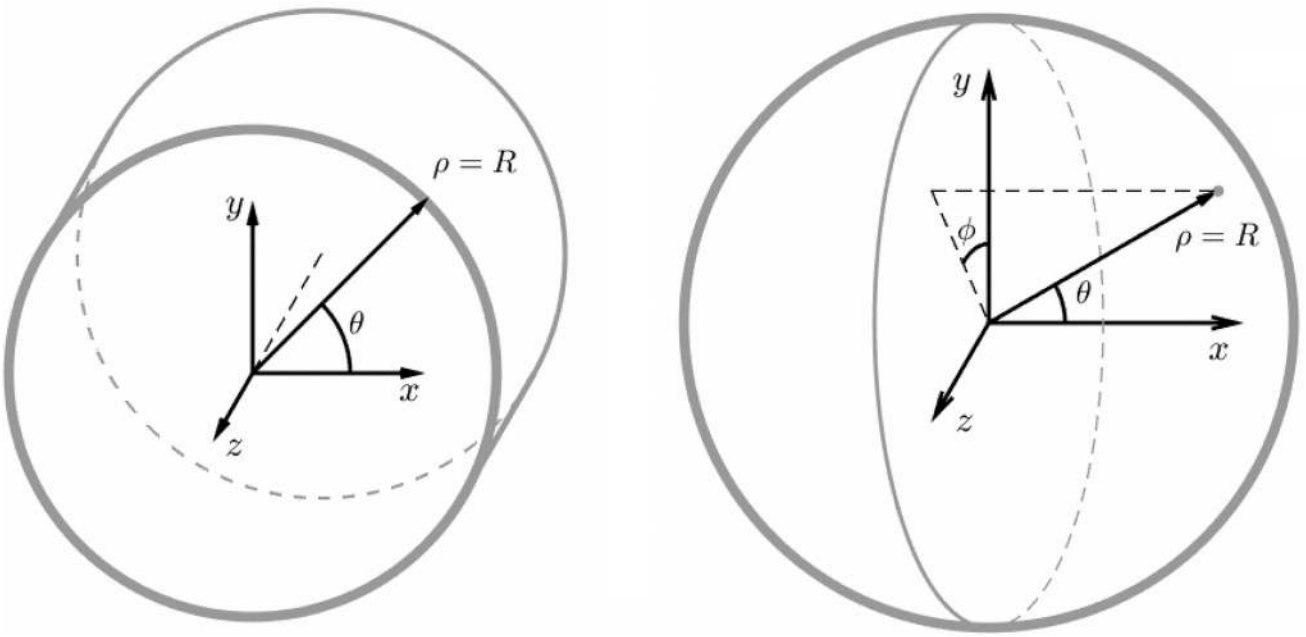

Figure 1.
Unified coordinate system for axons and somas. The local field orientation defines the x direction for both geometries. For the axon, the z direction is aligned with its axis. For the soma, the y and z directions and azimuth ϕ are arbitrary but are shown to be consistent with the axon.

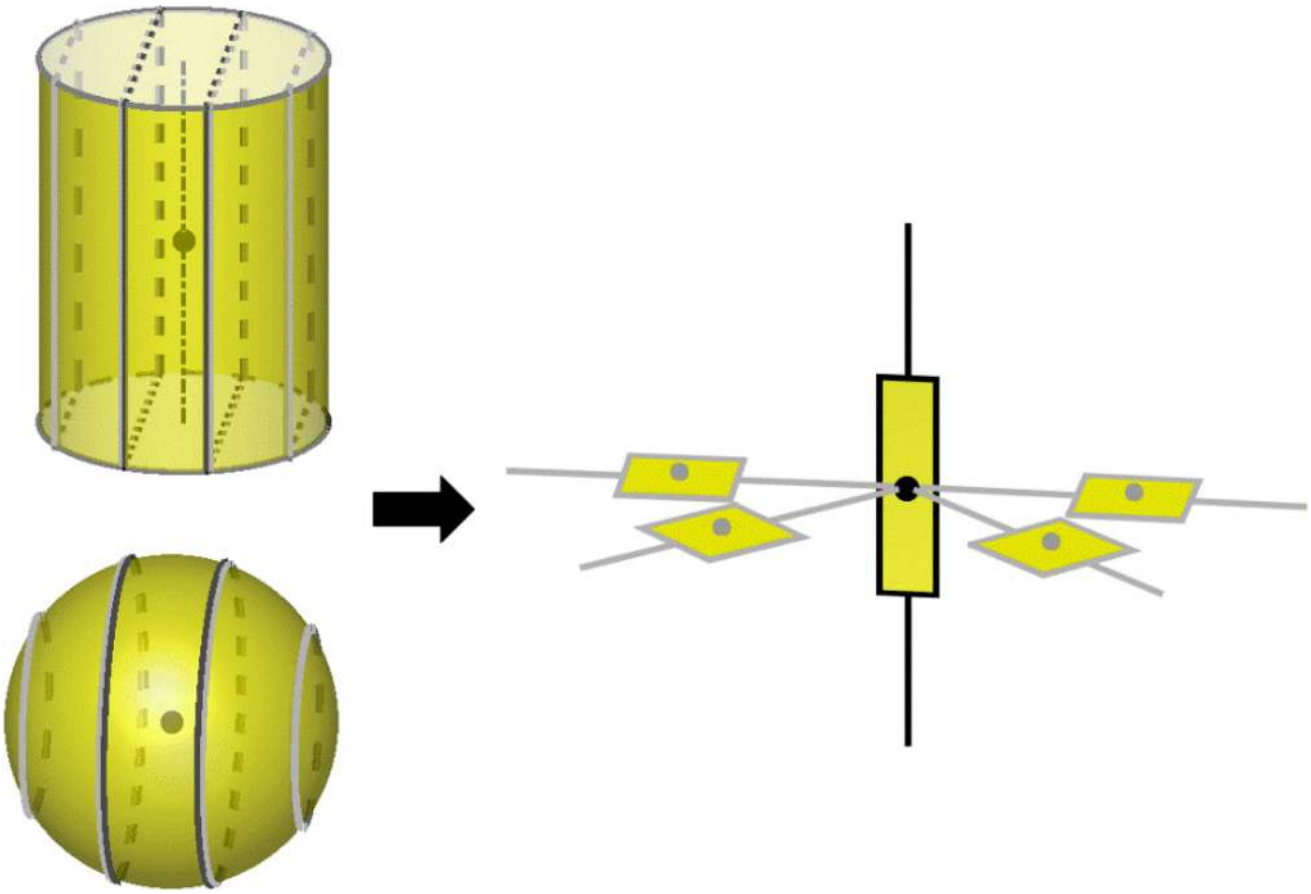

Figure 2.

The modified cable equation implementation in NEURON. Additional compartments are attached to each compartment subject to transverse field, forming the spoke-hub structure on the right with $N = 5$ and $M = 2$ shown as an example. For simplicity, the cylindrical compartments within the solver are represented as rectangles with their nodes shown as points and topological connections as lines. The black hub compartment retains the topological connection with adjacent compartments and holds the mean membrane potential in the modified cable equation. The spoke compartments represent the membrane modulated from the mean values by the transverse polarization resulting from the transverse field. Due to the negligible intracellular resistivity, any neurite connected to the soma can be attached at the node or either end of the hub.

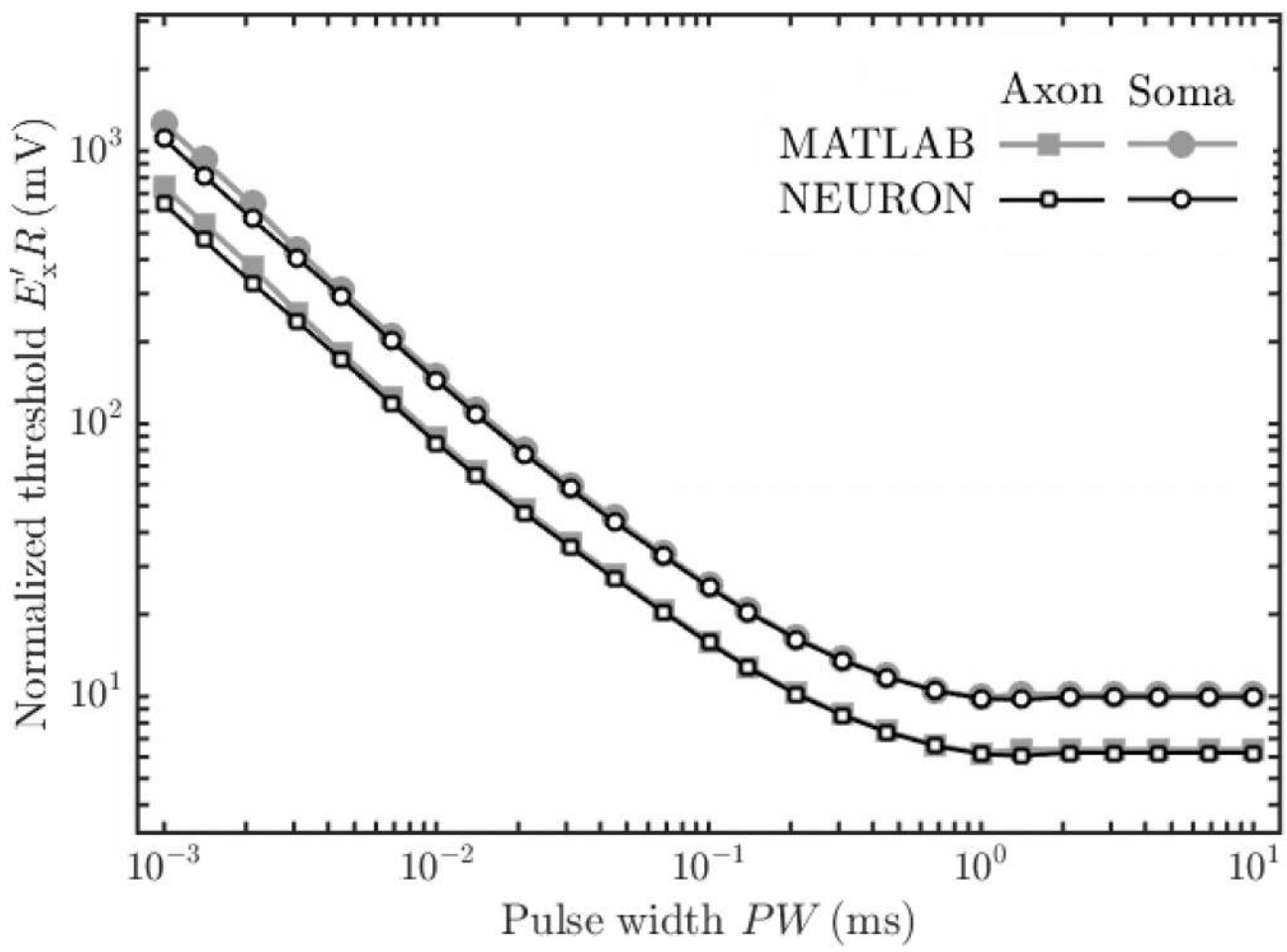

Figure 3.

Strength–duration curves on log–log scale for HH-type single compartments under transverse E-field. The threshold values are normalized for compartment radius and results are identical within geometry for different radii. See main text for discussion of discrepancy between the two implementation methods. The soma has about 60% higher thresholds than axon for a given radius. The log–log slope for short pulses is −0.79, different from the −1 slope for the integrate-and-fire model.

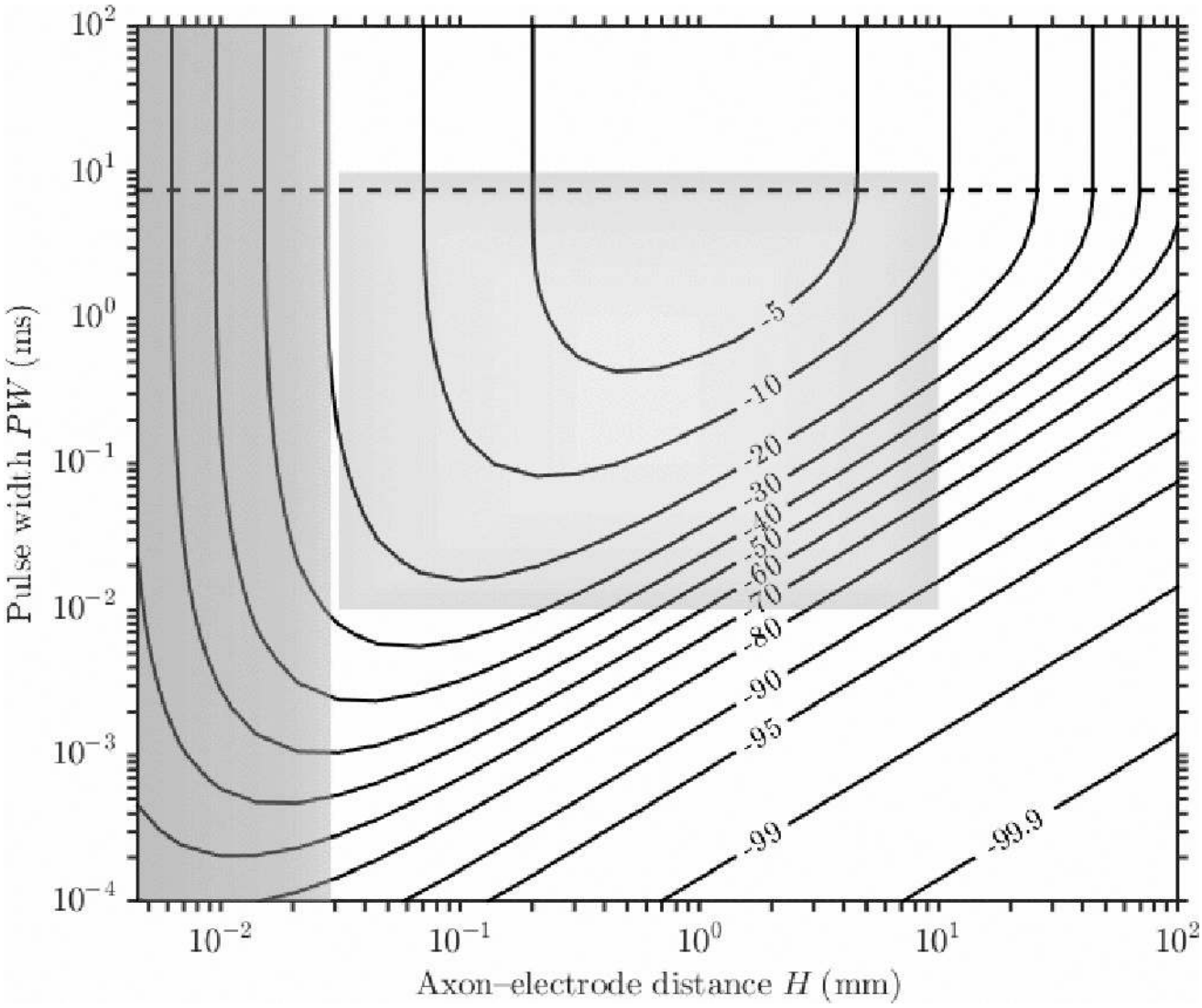

Figure 4.

Percentage difference in the maximum membrane depolarization between the conventional and the modified cable equations for a linear unmyelinated axon and point source model with cathodic current input. The contour lines indicate increasing influences of transverse polarization for shorter pulses or farther electrode placement. The dashed horizontal lines at about 7.5 ms indicates the pulse width to reach steady state for the membrane potential. The left shaded region indicates deviation from the analytical solution [28] in the near field where the assumption of uniform transverse field is invalid. The shaded region in the center outlines the parameter space of typical neural engineering applications using electrical stimulation.

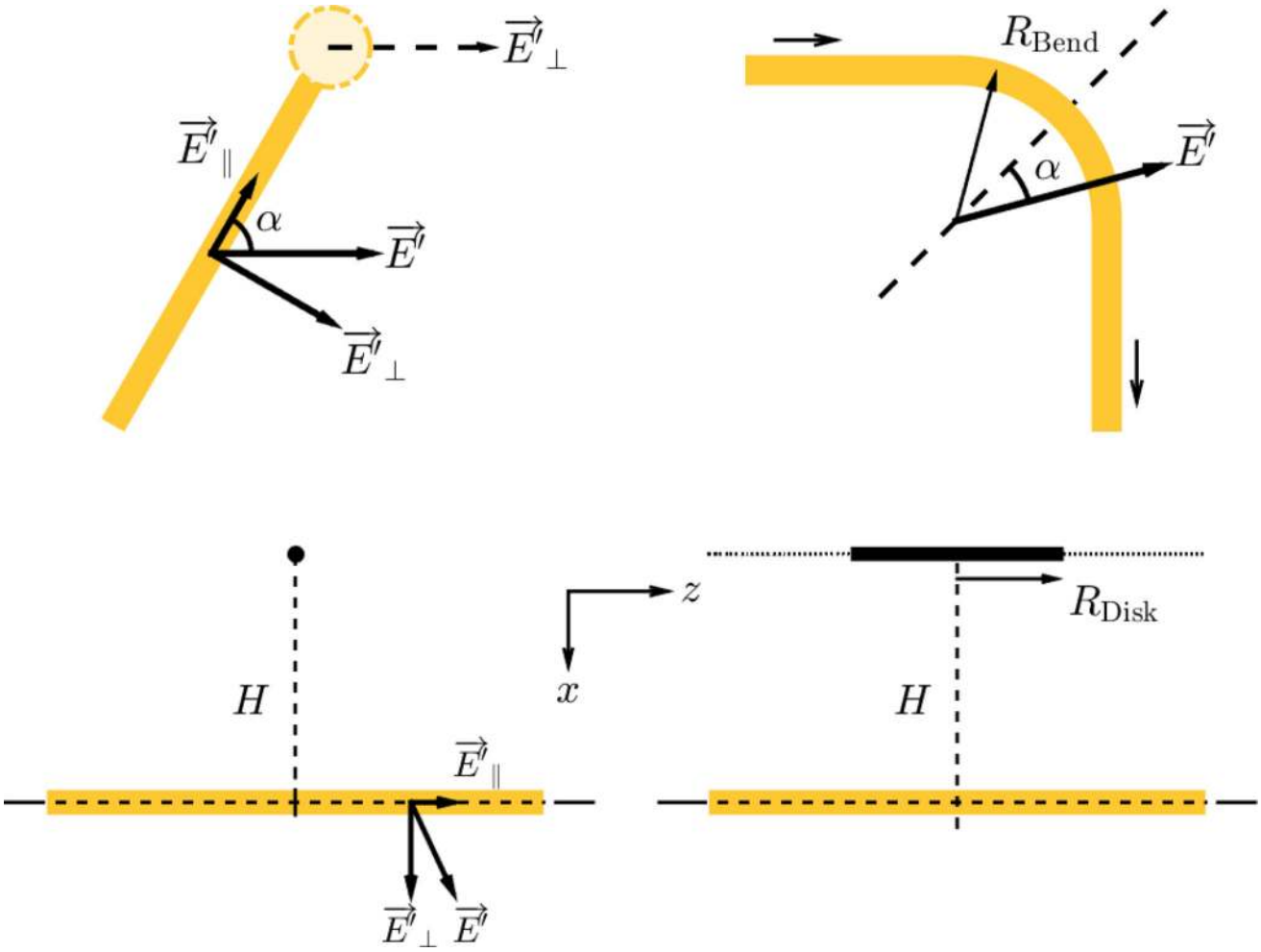

Figure 5.

Illustration of test scenarios for electrical stimulation. Top: semi-infinite axon with terminal (left) and infinite axon with bend (right) in uniform E-field. Bottom: infinite axon in E-field generated by point source (left) or disk (right) electrode.

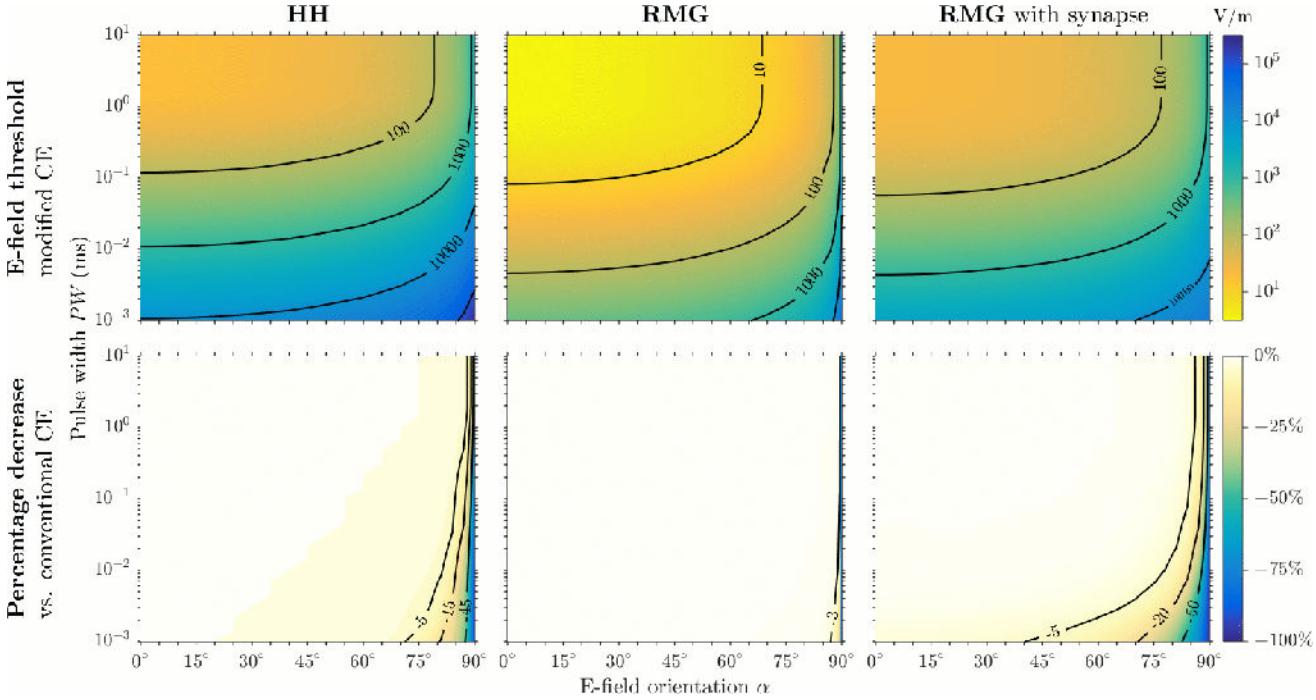

Figure 6.

Influence of transverse polarization on activation of axon terminals under uniform E-field. Top row: threshold values obtained with modified cable equation. Bottom row: percentage change of threshold compared with conventional cable equation.

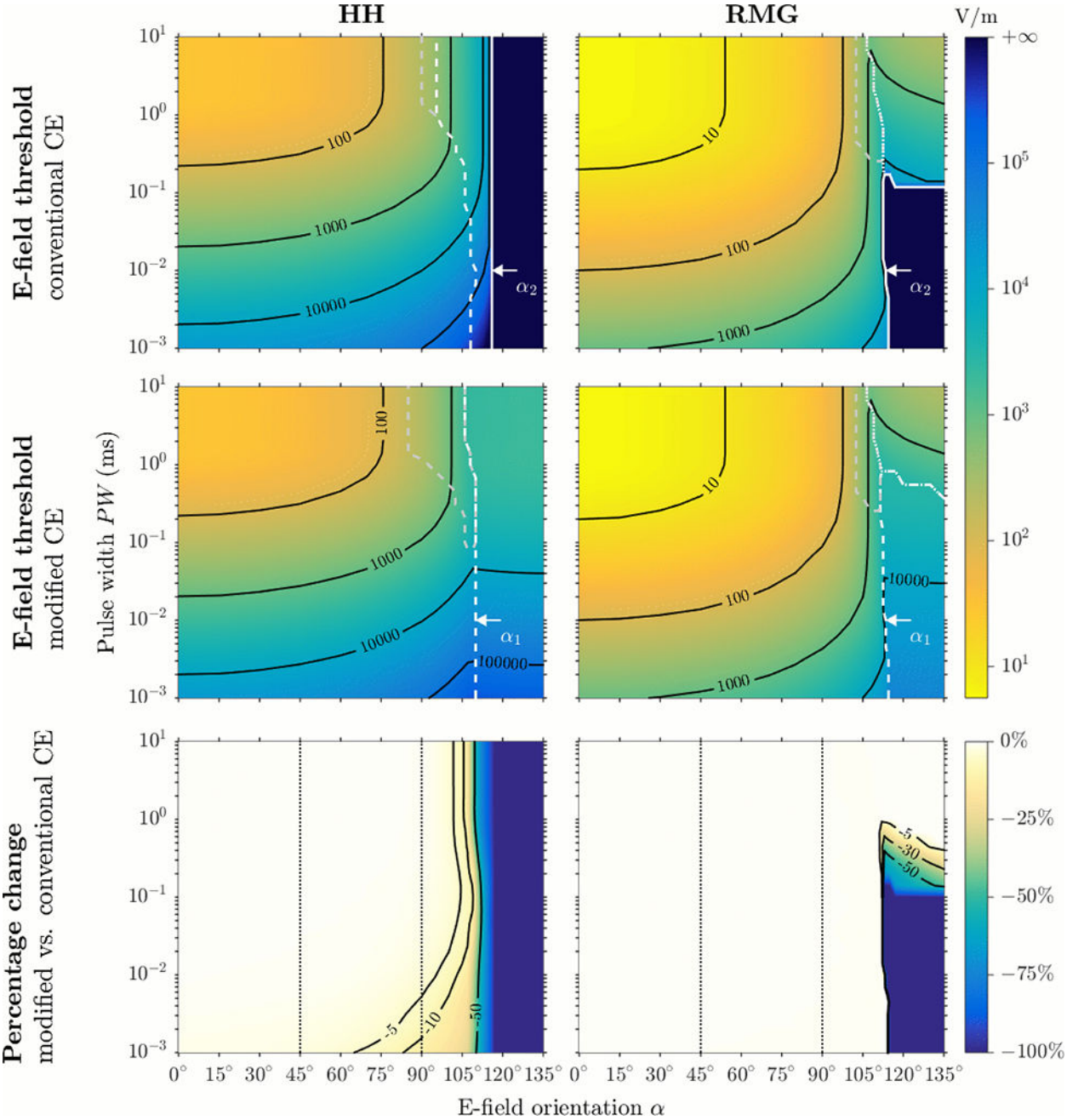

Figure 7.

Influence of transverse polarization on activation of axonal bends under uniform E-field. Top and middle rows: threshold values obtained with conventional and modified cable equations, respectively. The dashed and solid white/gray lines delineate parameter boundaries for different behaviors of the models (see main text for discussion). Bottom row: percentage decrease of threshold of modified cable equation. The dotted vertical lines separate field orientations into three categories: into the bend (0°–45°), inward tangent (45°–90°) and outward tangent to the bend (90°–135°).

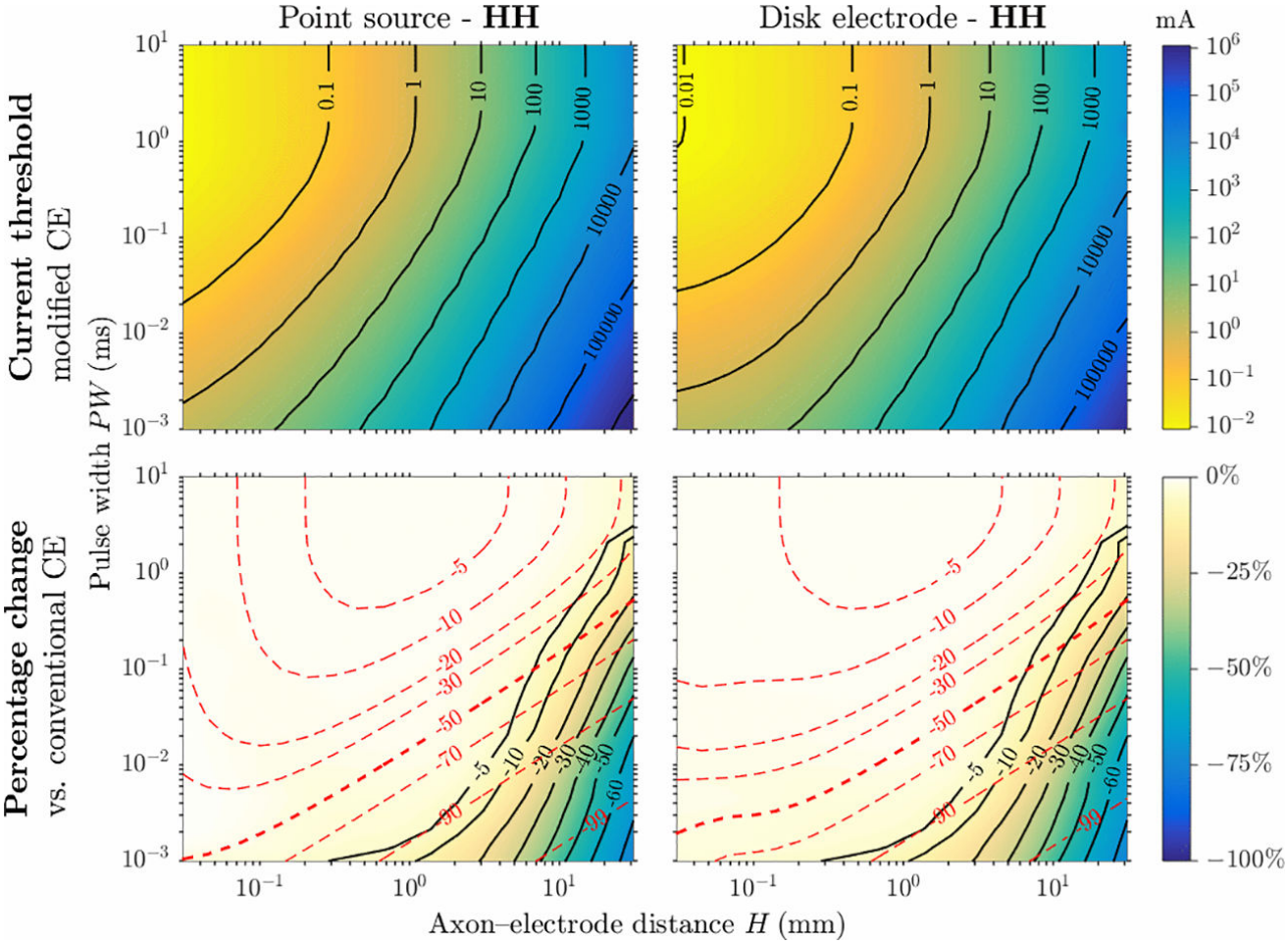

Figure 8.

Activation of axons by point source (left column) and disk electrodes (right column) for the HH model. Top row: threshold values obtained with the modified cable equation. Bottom row: percentage decrease of threshold compared with conventional cable equation is shown as solid contour lines, with percentage difference in maximum linear depolarization overlaid as dashed lines.

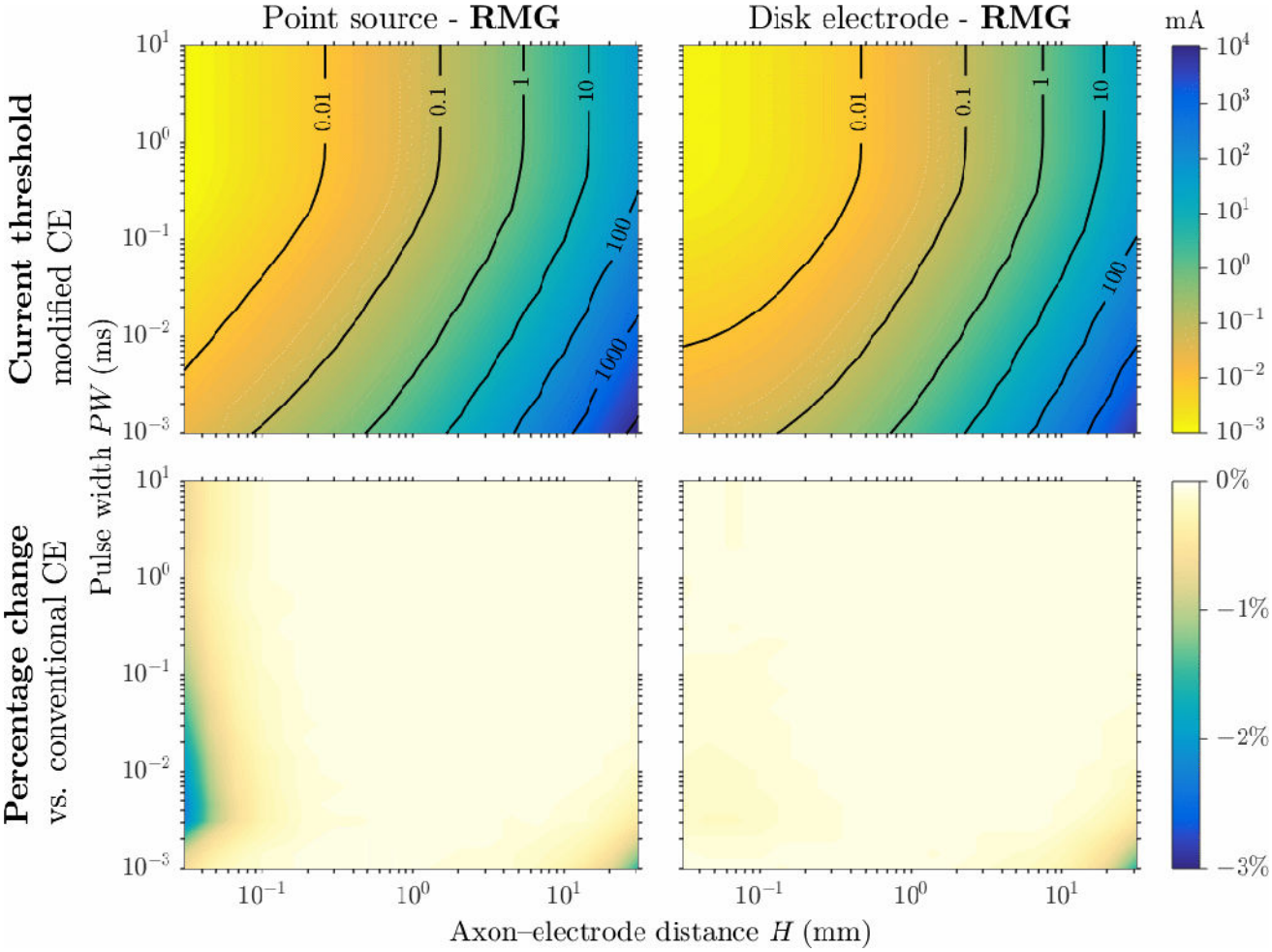

Figure 9.

Activation of axons by point source (left column) and disk electrodes (right column) for the RMG model. Top row: threshold values obtained with modified cable equation. Bottom row: percentage change of threshold compared with conventional cable equation (note different color scale compared to Figure 6–8).

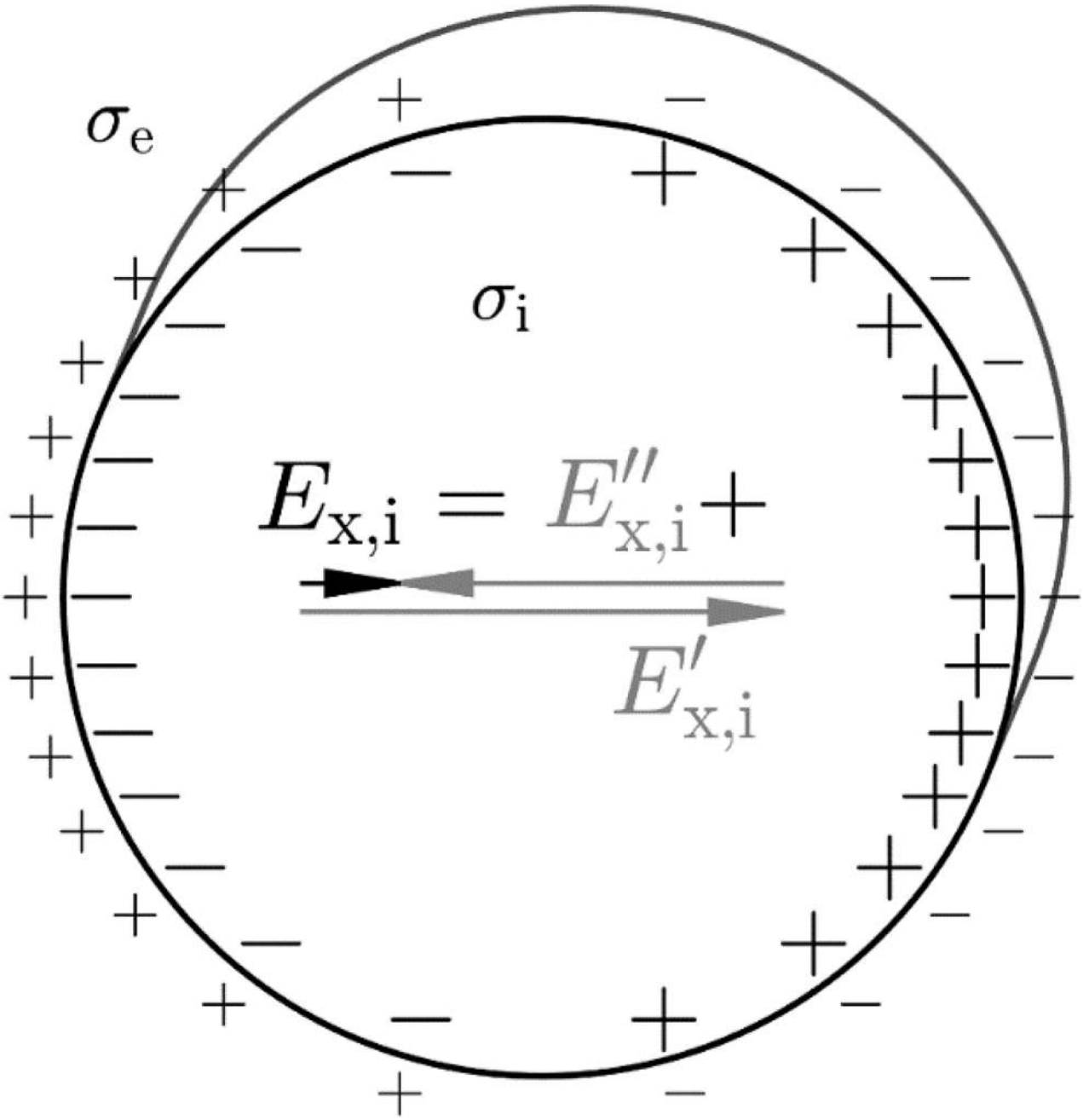

Figure 10.

The steady state polarization of the membrane and intracellular space after transverse depolarization. The bi-directional charge redistribution through the intra- and extra-cellular spaces (with τ_c time scale) hyperpolarizes and depolarizes the anodal and cathodal membrane, respectively. Polarization also occurs through the local membrane resistance with τ_m time scale. The secondary intracellular field is opposite in direction to the applied field and almost entirely cancels out the applied field, leaving a residual field with a relative magnitude ϵ at steady state. The vector lengths are exaggerated for illustration purpose. The

mismatched sizes of the "+" and "–" symbols represent the stored charge, with $\sigma_i > \sigma_e$ assumed; for $\sigma_i < \sigma_e$ the size relationship is reversed.

Table I

Parameters for the N compartments in the multicompartment structure modeling transverse polarization shown in Figure 2.

Parameters[a]	Axon	Soma
Surface area[b]	$\frac{1}{N}$	$\frac{\pi}{2N}\sin\ \theta_{b}$[c]
Axial resistance[b]	1 (hub) or 0[d] (spokes)	0[d]
Extracellular potentials	$\overline{\varphi}_{\mathrm{e}}^{'} - 2E_{\mathrm{x}}^{'}R\ \cos\ \theta_{b}$	$\overline{\varphi}_{\mathrm{e}}^{'} - \frac{3}{2}E_{\mathrm{x}}^{'}R\ \cos\ \theta_{b}$

[a] See (20) for definition of angles θ_b and indices b. Hub and spoke compartments correspond to $b = 0$ and $b \neq 0$, respectively.

[b] Values given as fraction compared to the parameters of the original compartment. Implementation is non-unique and can be achieved by various combinations of compartment length, diameter, and intracellular resistivity.

[c] Exact ratio is $\sin\frac{\pi}{2N}\sin\ \theta_{b}$.

[d] Or a negligible value, e.g., 10^{-3}, to avoid numerical issues within the solver.

Table II

Simulation parameters for unmyelinated axon and point source electrode.

Intracellular conductivity	σ_i	28.3 mS/cm
Extracellular conductivity	σ_e	10 mS/cm
Axon radius	R	3 μm
Current amplitude	I	−2 mA
Axon–electrode distance	H	4.5 μm–10 cm
Pulse width	PW	0.1 μs–100 ms

Table III

Axon parameters of myelinated axon.

Parameter	Units	Node	Internode
R	μm	1.65	3
L	μm	1	1150[a]
c_m	nF/cm^2	2000	0.42
r_m	kΩ·cm^2	0.096[b]	240
σ_i	mS/cm	14.3	14.3
σ_e	mS/cm	2	2

[a] Total length of 10 compartments.

[b] At rest.

Table IV

Ion channel parameters for the HH and RMG axon models.

Parameter	Symbol	Units	HH	RMG
Maximum Na^+ conductance	g_{Na}	mS/cm^2	120	3000
Maximum persistent Na^+ conductance	g_{Nap}	mS/cm^2	–	5
Maximum K^+ conductance	g_K	mS/cm^2	36	80
Leakage conductance	g_L	mS/cm^2	0.3	80
Resting potential	V_r	mV	−65	50
Na^+ reversal potential	$\mathcal{E}_{Na}$	mV	50	50
K^+ reversal potential	$\mathcal{E}_K$	mV	−77	−84
Leakage reversal potential	$\mathcal{E}_L$	mV	−53.39	−83.28
Simulation temperature	T	°C	23.5	37